

RESEARCH ARTICLE

Observation and simulation of mountain wave turbulence above Iceland: Turbulence intensification due to wave interference

Henrike Wilms¹  | Martina Bramberger^{1,2} | Andreas Dörnbrack¹

¹Deutsches Zentrum für Luft- und Raumfahrt, Institut für Physik der Atmosphäre, Oberpfaffenhofen, Germany

²now at: NorthWest Research Associates, Colorado Research Associates Division, Boulder, Colorado

Correspondence

H. Wilms, German Aerospace Center, Münchener Straße 20, Weßling 82234, Germany.

Email: henrike.wilms@dlr.de

Funding information

Deutsche Forschungsgemeinschaft, Grant/Award Numbers: GW-TP/DO 1020/9-1, PACOG/RA 1400/6-1

Abstract

The High-Altitude Long Range research aircraft (HALO) encountered strong turbulence above Iceland at 13.8 km altitude on 13 October 2016. The generation of turbulence along the flight path is studied through numerical simulations in combination with the aircraft *insitu* observations. From the *insitu* observations, maximum energy dissipation rate values (cube root of the energy dissipation rate) of $0.39 \text{ m}^{2/3} \cdot \text{s}^{-1}$ are obtained, which correspond to moderate to severe turbulence for a medium-weight aircraft such as HALO. The turbulent region is characterized by observed large-amplitude vertical wind fluctuations which coincide locally with a stagnation of the horizontal flow. The strong turbulence occurred downstream of and between the two Icelandic mountains Hofsjökull and Langjökull. High-resolution numerical simulations, with realistic and idealized topography, show that the flow above these two nearby mountains is responsible for the observed turbulence. Vertically propagating hydrostatic mountain waves disperse horizontally in the region downstream and between Hofsjökull and Langjökull. There, both waves interfere and their superposition leads to enhanced amplitudes and, eventually, to convective instabilities. By comparing simulations with only one of the mountains to the simulation with both mountains, we infer that the wave interference can locally amplify the turbulence intensity by a factor of five and double the vertical extent of the turbulent region.

KEYWORDS

mountain waves, turbulence, wave breaking, wave interference

1 | INTRODUCTION

Turbulence in the atmosphere is considered to be among the major hazards for commercial aircraft at cruising

altitudes between 8 and 14 km (Tvaryanas, 2003; Lane *et al.*, 2009; Sharman *et al.*, 2012b). There are various sources for turbulence in the upper troposphere and lower stratosphere, among which are breaking gravity

This is an open access article under the terms of the Creative Commons Attribution-NonCommercial-NoDerivs License, which permits use and distribution in any medium, provided the original work is properly cited, the use is non-commercial and no modifications or adaptations are made.

© 2020 The Authors. *Quarterly Journal of the Royal Meteorological Society* published by John Wiley & Sons Ltd on behalf of the Royal Meteorological Society.

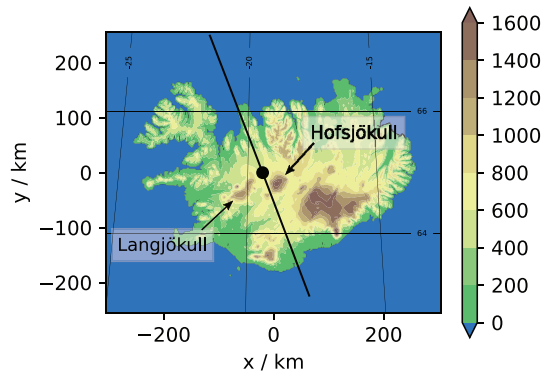


FIGURE 1 Orography of Iceland (in m) with the two mountains Hofsjökull and Langjökull. The thick black line represents the HALO flight track with the turbulence encounter at the position of the black dot. The thin lines show longitude and latitude

waves, strong wind shears associated with jet streams and upper-level fronts, unbalanced flow as well as thunderstorms (Sharman *et al.*, 2012b, and reference therein). The contribution of gravity waves to atmospheric turbulence is two-fold. On the one hand, gravity waves may locally reduce the Richardson number below a critical threshold which then causes turbulence due to dynamic instabilities (Pavelin *et al.*, 2001; Lane *et al.*, 2004; Koch and *et al.*, 2005). On the other hand, large-amplitude gravity waves are prone to overturning which leads to turbulence due to convective instabilities. Turbulence associated with mountain waves is termed mountain wave turbulence. Regions particularly susceptible to mountain wave turbulence are the Rocky Mountains (Wolff and Sharman, 2008), the Alps (Schmid and Dörnbrack, 1999; Jiang and Doyle, 2004), and Greenland (Doyle *et al.*, 2005; Lane *et al.*, 2009; Ólafsson and Ágústsson, 2009; Sharman *et al.*, 2012a).

During the North Atlantic Waveguide and Downstream Impact Experiment (NAWDEX; Schäfler *et al.*, 2018) the High Altitude and Long range research aircraft HALO encountered strong turbulence above Iceland. The turbulence encounter occurred on 13 October 2016 close to two isolated mountains, namely the Hofsjökull mountain and the Langjökull glacier (Figure 1). HALO was flying between these two mountains, when the turbulence encounter occurred approximately 30 km downstream of the two mountain peaks.

This turbulence encounter was already analyzed by Bramberger *et al.* (2020). They combined the HALO *in situ* observations and *in situ* observations from the coordinated flight of the French Falcon from SAFIRE (Service des Avions Français Instrumentés pour la Recherche en Environnement) with 2D numerical simulations along the flight track. With these data they were able to explain turbulence at flight levels close to the observed turbulence

due to overturning hydrostatic mountain waves. However, in their simulations, the horizontal position of the turbulence is directly above the mountain peak and not downstream, as in the observations.

We therefore raise the following question: what caused the horizontal displacement of the observed turbulence relative to the mountain peaks? We hypothesize that waves excited by the two mountains also dispersed horizontally, interfered, and broke in the region between. This could be the location where HALO encountered the turbulence.

The interaction and interference of mountain waves and their stability has previously been studied analytically (Grisogono *et al.*, 1993; Lee *et al.*, 2006), numerically (Vosper, 1996; Mayr and Gohm, 2000; Sharman and Wurtele, 2004; Grubišić and Stiperski, 2009; Stiperski and Grubišić, 2011) and in water tank experiments (Gyüre and János, 2003; Stiperski *et al.*, 2017). All these studies employed mountains that were distributed in the direction of the flow. However, hydrostatic mountain waves excited by isolated peaks also disperse horizontally (Smith, 1980). Thus, flow across isolated mountains aligned laterally to the flow will excite waves which interfere downstream of their summits. The interference and interaction of laterally dispersing mountain waves has so far – to the best of our knowledge – not been studied in tank experiments or numerical studies. In this sense, this case-study expands on previous investigations of the flow over double-mountain topography, but for mountains arranged laterally with respect to the mean flow.

Satellite observations of tropospheric water vapour reveal that complex wave structures, interference patterns or crossing wave fronts are associated with stronger turbulence (Uhlenbrock *et al.*, 2007). In a recent study, van der Mescht and Geldenhuys (2019) even relate interfering mountain waves to a fatal aircraft crash over South Africa.

In addition to the hypothesis that wave interference led to the observed turbulence, three further possible explanations for turbulence downstream of the mountain peaks will be addressed in this study:

1. Dynamic instabilities could have been generated in the strong shear zone above the jet streak where HALO was flying. This could have been the cause of the observed turbulence. Additionally, the background shear could have been amplified by mountain waves.
2. The turbulence could have been advected by the mean wind, leading to the observed turbulence downstream of the mountain wave breaking region.
3. The orography data used in the study of Bramberger *et al.* (2020) has a rather coarse resolution (~ 8 km). With this resolution, smaller mountains in the vicinity of Hofsjökull and Langjökull are not resolved, which

could have lead to the mismatch between the observed and simulated turbulence position.

With numerical simulations and their comparison to the HALO *in situ* observations, we analyze the effects leading to the downstream displacement of the breaking region. The simulations build upon the results presented in Bramberger *et al.* (2020). We advanced the model set-up by extending the simulation domain to three dimensions and using a finer resolved orography. The remainder of the paper is organized as follows. The airborne *in situ* observations are presented in Section 2. Section 3 introduces the numerical model EUALG, including the set-up for the simulations. Section 4 presents the simulations, which are discussed in Section 5. A conclusion evaluating the four above stated explanations follows in Section 6.

2 | RESEARCH FLIGHT 10 OF NAWDEX CAMPAIGN

The NAWDEX campaign took place in September and October 2016 in Iceland (Schäfler *et al.*, 2018). During a research flight on 13 October 2016, HALO encountered strong turbulence at 65.0°N, 19.4°W (above central Iceland) at 13.8 km altitude at 1453 UTC. A detailed analysis of the *in situ* data and the meteorological situation is presented in Bramberger *et al.* (2020). Here, we only briefly summarize the aspects which are important for the following analysis.

During 13 October 2016, the tropospheric winds above Iceland were predominantly southerly. The surface winds exceeded 10 m·s⁻¹ upstream of Iceland. The polar front jet at 300 hPa was almost perfectly aligned with the surface winds, so that there was little directional wind shear. The HALO flight track was located to the east of the jet streak and approximately 3.5 km above the altitude of maximum winds in a region of negative vertical shear. The orientation of the flight track deviated by about 2° from the jet direction and was thus almost parallel. HALO was flying southwards, but note that in the following, all data along the flight track are presented with positive x-axis in the flow direction, that is, towards the north.

HALO *in situ* measurements of wind and temperature are shown in Figure 2. The high-resolution measurements have a temporal resolution of 10 Hz which translates to a horizontal resolution of ≈ 25 m. The data were spectrally filtered to 1 Hz resolution for Figure 2. The spatial resolution of the measurements is sufficiently high to well resolve the velocity extrema in Figure 2. From the three wind components, the cube root of the energy dissipation rate (EDR) ϵ (with $\text{EDR} = \sqrt[3]{\epsilon}$) was calculated according to the method described in Bramberger *et al.* (2018). The calculation of EDR was performed with

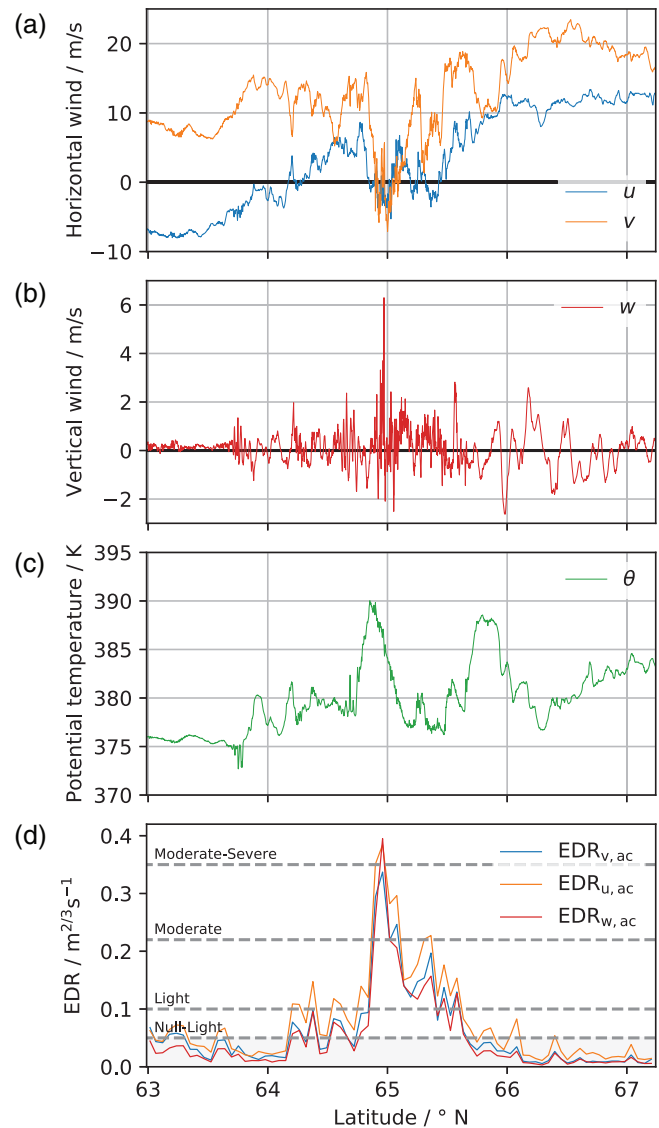


FIGURE 2 HALO *in situ* measurements along the flight track of (a) zonal wind (blue) and meridional wind (orange), (b) vertical wind and (c) potential temperature. (d) shows energy dissipation rate (EDR) derived from the three velocity components in aircraft coordinates

velocity perturbations in the aircraft coordinate system, that is, u_{ac} is the longitudinal (along-track) and v_{ac} the transverse (cross-track) velocity component. Velocity fluctuations between 0.1 and 3.5 Hz contributed to the EDR calculation.

EDR along the flight track is shown in Figure 2d. The thresholds for turbulence categories for a medium-weight aircraft such as HALO are based on Sharman *et al.* (2014).

Enhanced EDR values are found between 64.2° and 66.1°N. With peak values of $\text{EDR}_{\max} = 0.39 \text{ m}^{2/3} \cdot \text{s}^{-1}$ at around 65°N, this event falls into the category of moderate to severe turbulence (Sharman *et al.*, 2014). This event of strong turbulence was accompanied by large variations in the vertical wind, with a maximum amplitude of 6.3 m·s⁻¹

(Figure 2b). The region between 64.8° and 65.2°N was characterized by a sudden decline in the meridional wind v by $\sim 20\text{ m}\cdot\text{s}^{-1}$ and a subsequent recovery (Figure 2a). The zonal wind exhibited two smaller drops of $\sim 12\text{ m}\cdot\text{s}^{-1}$. Both wind components exhibited a sign change, i.e. a wind reversal, close to the position of the maximum EDR value. A peak in potential temperature was found slightly upstream of the turbulence event, with a second peak of similar amplitude further downstream (Figure 2c).

3 | THE NUMERICAL MODEL EULAG

In this study we present numerical simulations with the multiscale geophysical flow solver EULAG (Eulerian/semi-Lagrangian fluid solver; Prusa *et al.*, 2008). EULAG has been used to model geophysical flows across a wide range of scales and applications from boundary-layer turbulence and clouds (e.g., Pedersen *et al.*, 2018) to gravity wave propagation and breaking (Prusa *et al.*, 1996; Smolarkiewicz and Margolin, 1997) and as a dynamical core for regional weather modelling (Kurowski *et al.*, 2016).

The model set-up employed in this study solves the non-hydrostatic anelastic equations (Ogura and Phillips, 1962; Lipps and Hemler, 1982) in generalized coordinates. The formulation of the governing equations in generalized coordinates allows for irregularly spaced grids in physical space, i.e. for local grid refinement which yields higher resolutions in desired areas. The detailed model equations can be found in Appendix A.

3.1 | Model domain

Three different numerical simulations are presented in this study. The domain of the first simulation is two-dimensional (2D) and oriented along the HALO flight path. The second simulation is three-dimensional (3D) and comprises the complete island of Iceland. The third simulation, also 3D, has a simplified topography and the area around the turbulence encounter is resolved with a finer grid, which is achieved by horizontal grid stretching. The three simulation domains are depicted in Figures 1 and 3.

The first domain along the flight path has a horizontal extent of 576 km and a horizontal resolution of 2 km. In the vertical the model extends from the surface to a height of 25 km with a vertical resolution of 100 m. The orography for this domain is extracted from the global relief model (ETOPO1; Amante and Eakins 2009) by linear interpolation onto the flight path (Figure 3a). We refer to this domain as Iceland 2D.

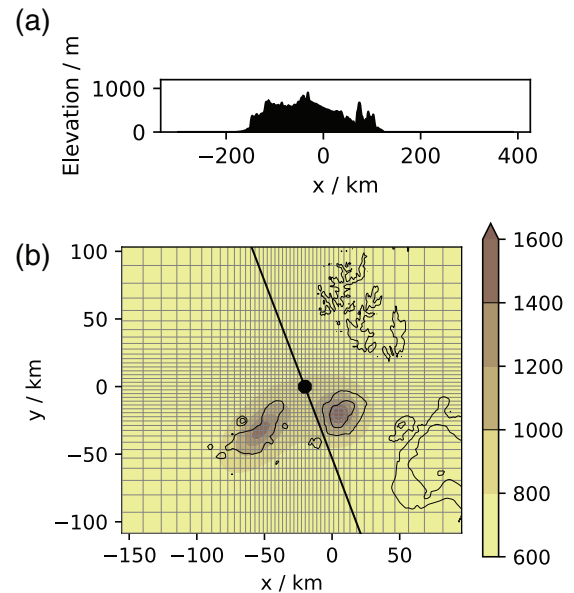


FIGURE 3 Orography of (a) Iceland 2D domain and (b) double-mountain domain (in m). In (b) the thick black line shows the HALO track with the turbulence encounter at the position of the black dot, the thin black lines are the 1,000 and 1,400 m elevation levels from the high-resolution topography ETOPO1, and the thin grey lines show every 8th grid line to visualize the grid stretching

The second domain, Iceland 3D, has a horizontal extent of $612 \times 512\text{ km}$ with a horizontal resolution of $2 \times 2\text{ km}$. As for the Iceland 2D domain, the orography is generated by linearly interpolating ETOPO1 onto the computational grid of EULAG, using the sinusoidal projection (also called Mercator equal-area projection) with the central meridian at 19°W . The Iceland 3D domain with its topography is shown in Figure 1. The origin of the domain corresponds to 65°N , 19°W and the turbulence encounter occurred at $x = -17.5\text{ km}$ and $y = -6.8\text{ km}$.

The third domain is named the "double-mountain domain", because the orography consists of two idealized mountains. The mountain southeast of the turbulence event, Hofsjökull, is known for its almost perfect bell-shaped form (Reuder *et al.*, 2012). This mountain is therefore replaced by an analytically defined function describing a so-called Witch of Agnesi. The other mountain ridge southwest of the turbulence event (which is covered by the Langjökull glacier) is replaced in a similar manner by a Witch of Agnesi mountain which is stretched in a diagonal direction. The idealized orography of the third domain is thus described by a superposition of the mountain to the east (\mathcal{M}_E) and the mountain ridge to the west (\mathcal{M}_W) on top of a plateau

$$h(x, y) = h_0 + \mathcal{M}_E(x, y) + \mathcal{M}_W(x, y) \quad (1)$$

TABLE 1 Parameters describing the double-mountain topography

	\mathcal{M}_E	\mathcal{M}_W
Mountain height A_i (m)	1,150	900
Mountain half-width $s_{x,i}, s_{y,i}$ (km)	10.5, 10.5	20.0, 10.5
Lateral displacement $x_{0,i}, y_{0,i}$ (km)	4.9, -20.0	-52.8, -32.5
Tilting angle γ_i (degrees)	0	45
Plateau height h_0 (m)	600	

with the individual mountains $\mathcal{M}_i(x, y)$ described by

$$\mathcal{M}_i(x, y) = \frac{A_i}{1 + B_{x,i}^2 + B_{y,i}^2} \quad (2)$$

and

$$B_{x,i} = \frac{(x - x_{0,i}) \cos \gamma_i + (y - y_{0,i}) \sin \gamma_i}{s_{x,i}}, \quad (3)$$

$$B_{y,i} = \frac{(y - y_{0,i}) \cos \gamma_i - (x - x_{0,i}) \sin \gamma_i}{s_{y,i}}. \quad (4)$$

Table 1 lists the parameters of \mathcal{M}_W and \mathcal{M}_E , namely the mountain peak heights A_i , the mountain widths $s_{x,i}$ and $s_{y,i}$, zonal and meridional displacements of the mountains $x_{0,i}$ and $y_{0,i}$, as well as the tilting angle γ_i . The origin of the domain is the same as for the Iceland 3D domain, so that the position of the turbulence encounter is at $x = -17.5$ km and $y = -6.8$ km. Both mountains are placed on a plateau with height h_0 . This was necessary because the real topography has a gentle slope which falls off towards the coast over 100 km. For simplicity,

the slope was replaced by a constant value h_0 which reflects the mean elevation around the two mountains. The double-mountain domain is shown in Figure 3b. The comparison with the ETOPO1 elevation levels demonstrates that \mathcal{M}_E , the circular mountain to the east of the flight track, closely resembles the real orography, whereas \mathcal{M}_W is only a simplified approximation of the underlying orography.

The double-mountain domain has on average a horizontal resolution of 700 m with 360 (306) grid points in the x - (y -) directions. To increase the resolution in the region of the turbulence event, the grid has been refined to yield a resolution of 350 m close to the centre of the domain. The stretched grid is shown in Figure 3b with grey lines. The equations describing the grid stretching are documented in Appendix B. After 1 hr of model integration time, a restart with reduced time-step is performed to ensure Courant numbers below 1 (the maximum Courant number is 0.6 throughout the whole simulation). The above-mentioned parameters for all three domains are summarized in Table 2, which also includes the parameters of the damping layer at the top and lateral boundaries of the modelling domain, which are explained in more detail in the Appendix.

3.1.1 | Initial and boundary values

EULAG is initialized with horizontally homogeneous fields of horizontal wind and potential temperature based on the operational analysis of the European Centre for Medium-Range Weather Forecasts (ECMWF) Integrated Forecast System (IFS). The initialization profiles are extracted from the ECMWF operational analysis of 13 October 2016 at 1200 UTC at a position upstream of the island. Since HALO's flight track is almost antiparallel to

TABLE 2 Summary of modelling domain parameters

	Iceland domain 2D	Iceland domain 3D	Double-mountain domain
Number of gridpoints			
n_x, n_y, n_z	576, -, 251	306, 256, 142	360, 304, 251
Resolution			
dx, dy, dz (m)	2,000, -, 100	2,000, 2,000, 250	700, 700, 100
dt (s)	4	5	4 and 2
Topography	High-resolution 1D	High-resolution 2D	Idealized
Grid stretching	No	No	Yes
Absorber parameters			
$\delta x_{ab}, \delta y_{ab}, \delta z_{ab}$ (km)	50, -, 8	50, 28, 7.5	50, 30, 8
$\alpha_{0,x}, \alpha_{0,y}, \alpha_{0,z}$ (s^{-1})	200^{-1} , -, 180^{-1}	300^{-1} , 300^{-1} , 180^{-1}	200^{-1} , 200^{-1} , 180^{-1}

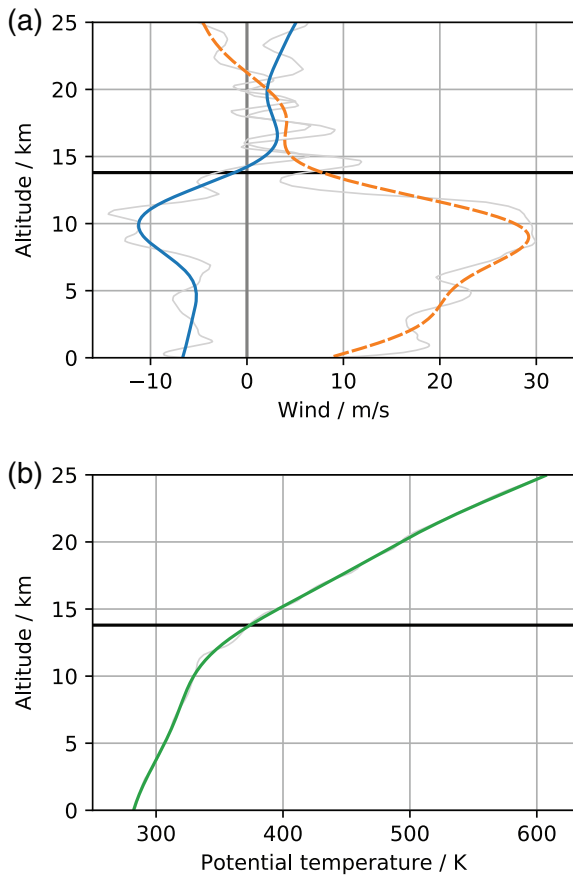


FIGURE 4 Environmental profiles for the numerical simulations. The profile for (a) u_e (solid), v_e (dashed) and (b) θ_e are extracted from ECMWF operational analysis at 1200 UTC on 13 October 2016, at the upstream position. Unfiltered ECMWF profiles are drawn as thin grey lines, and filtered profiles as bold lines

the wind direction at flight level (heading of the aircraft: 160° , wind direction: 170°), we take the upstream profile from a position along the flight track at 63.4°N . To remove any gravity waves which are resolved in the ECMWF operational analysis, the profile of both horizontal wind components and potential temperature are filtered with a fifth-order Butterworth filter and cut-off wavelength of 7.5 km. The original profiles and the filtered profiles are shown in Figure 4. The filtered profiles are used for the environmental profiles (u_e , v_e and θ_e ; Appendix A) and for the initialization profiles. For the Iceland 2D simulation, u_e is generated by projecting the horizontal wind onto the flight path and v_e is set to $0\text{ m}\cdot\text{s}^{-1}$.

The lateral boundary conditions are prescribed via the environmental profiles. Sponge layers at all lateral borders and the top relax the flow towards the environmental state and prevent wave reflections. The lower boundary is set to a free-slip condition for the velocity, and potential temperature perturbations are set to 0 K. All simulations presented in this study are performed without humidity.

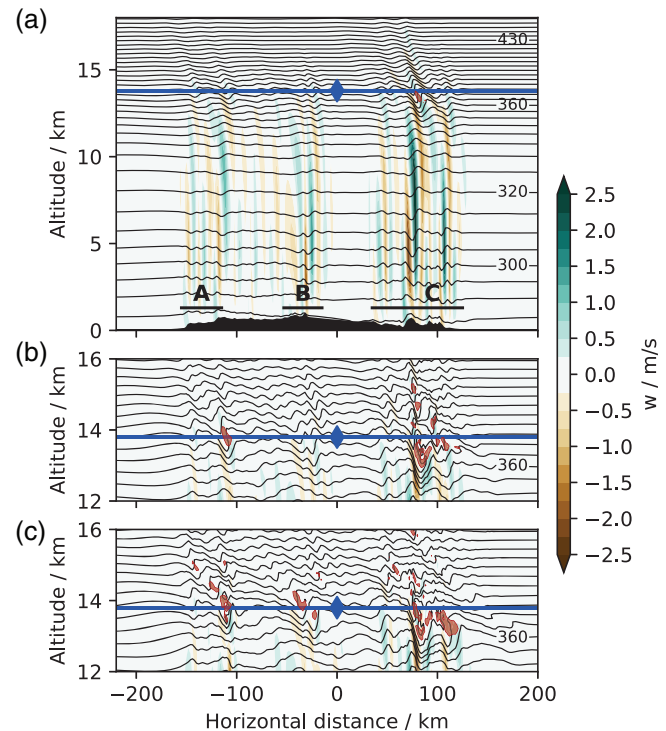


FIGURE 5 Vertical wind (color) and isentropes (black contours, in K) from Iceland 2D simulation for (a) $t = 1\text{ hr}$, (b) 2 hr and (c) 3 hr . The blue horizontal line shows the flight altitude of HALO and the blue diamond shows the position of the turbulence encounter. Red shaded regions indicate where $N^2 < 0$. Filled black area in (a) is the topography of the Iceland 2D domain

4 | SIMULATION RESULTS

4.1 | Iceland 2D domain

Figure 5 shows simulation results from the Iceland 2D domain at $t = 1, 2$ and 3 hr . Mountain waves are excited by mainly three regions with steep orography: the steep mountainsides close to the upstream coastline (A), the mountain peak on the central plateau with the highest elevation (B) and the group of mountains close to the downstream coast (C). The waves in region B have almost vertical phaselines in the troposphere. The stratospheric upstream tilt of the phase lines is associated with higher stratospheric stability and the strong shear above the jet streak (Figure 4). The waves excited in region C have the largest amplitudes (up to $3\text{ m}\cdot\text{s}^{-1}$) and become convectively unstable first as seen by the steep (Figure 5a) and overturning (Figure 5b, c) isentropes. Regions of negative stability, i.e. where the squared Brunt-Väisälä frequency $N^2 = (g/\bar{\theta})(d\bar{\theta}/dz)$ is negative, indicate overturning in this region (red shaded areas). Convective instabilities are also generated by the waves in region A at $t = 2\text{ hr}$ and in B at $t = 3\text{ hr}$. Over the course of the simulation, the wave amplitudes slightly amplify, but the prevailing wave pattern with

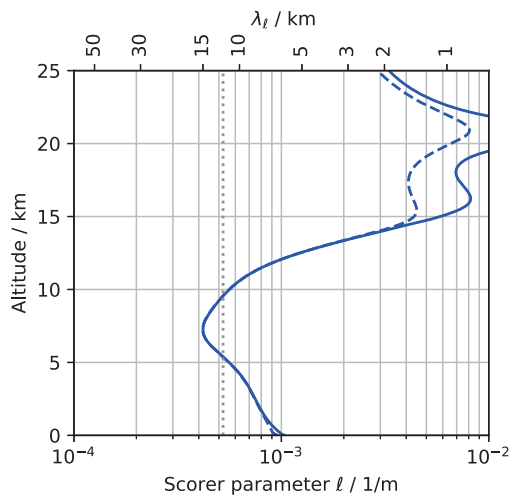


FIGURE 6 Scorer parameter ℓ derived from the environmental profiles. The solid line is calculated from the wind projected onto the flight path (as used in the Iceland 2D simulation) and the dashed line is calculated from the horizontal wind $U_h = \sqrt{u_e^2 + v_e^2}$. The dotted grey vertical line denotes the wavenumber of a wave with 12 km horizontal wavelength

three distinct sources persists. None of the three breaking regions occur directly at the position of the turbulence encounter (blue diamond in Figure 5). Waves excited in region B are the closest, but they break roughly 30 km upstream of the turbulence observations.

The dominant horizontal wavelength in region B, determined from a wavelet analysis of w at 5.5 km altitude (not shown), is 12 km. The Scorer parameter ℓ , with

$$\ell^2 = \frac{N^2}{U_h^2} - \frac{1}{U_h} \frac{d^2 U_h}{dz^2} \quad (5)$$

and U_h the horizontal wind, is shown in Figure 6. Waves with horizontal wave numbers larger than ℓ are evanescent. Thus, the 12 km wave in region B is evanescent in the altitude range between 5.5 and 9.5 km, which explains the vertical phase lines. The minimum ℓ indicates that all waves with horizontal wavelengths of 15 km or less encounter an evanescent layer in the troposphere. From linear theory, the amplitude of a mountain waves decreases in an evanescent layer according to $q = \exp(-\sqrt{k^2 - \ell^2} \Delta z)$ (e.g., Lin, 2007, chapter 5.2). Estimating an upper bound of the amplitude decrease for the 12 km wave by using the minimum Scorer parameter ($\ell = 4.2 \times 10^{-4} \text{ m}^{-1}$), $k = 2\pi/12 \text{ km}$ and $\Delta z = 4 \text{ km}$ as depth of the evanescent layer yields $q = 0.3$. This means that the wave amplitude decreases by a factor of 3 in the evanescent layer and the wave continues propagating above (wave leakage). Waves in region A experience a similar damping in the evanescent layer. In region C the wave spectrum is broader than in A and B. The dominant

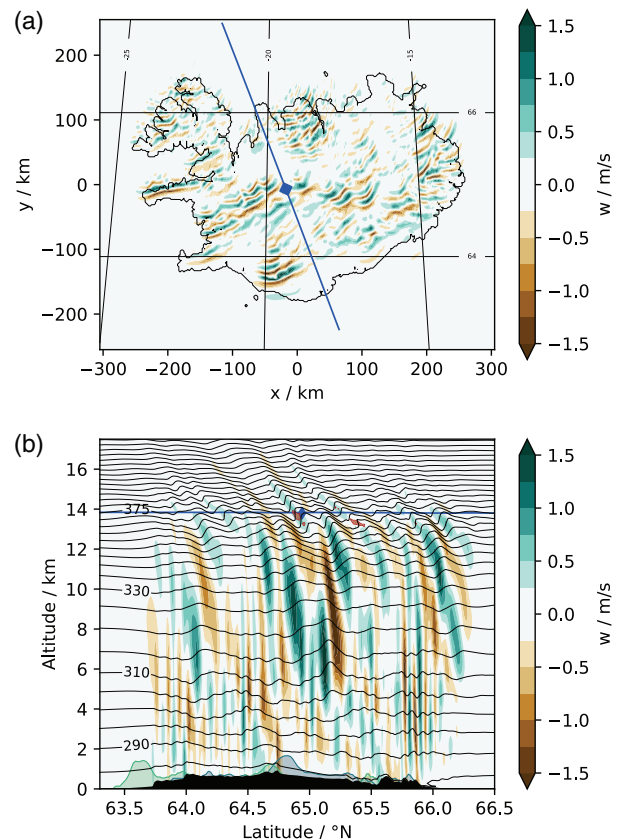


FIGURE 7 (a) Horizontal cross-section of w from Iceland 3D simulation at 13 km altitude at $t = 0.75 \text{ hr}$. (b) Cross-section along HALO flight track of w (colour) and isentropes (black contours, in K) at $t = 1.75 \text{ hr}$. The blue line indicates the flight track with the turbulence encounter at the position of the filled blue diamond. In (a) the thin black lines denote longitude and latitude. In (b) red shaded regions indicate where $N^2 < 0$. The black filled area is the topography along the flight track, the blue and green filled areas are the topography along cross-sections parallel to the flight track cutting through the peak of Hofsjökull and Langjökull

wavelength in C is also below 15 km, but additionally 25 km wavelength waves are found at 5.5 km altitude. This 25 km wavelength wave is able to propagate freely through the troposphere and becomes the dominant wavelength at 9.5 km altitude. As this wave does not experience any damping, it has the largest amplitudes and becomes convectively unstable first.

4.2 | Iceland 3D domain

A horizontal cross-section of the vertical wind field from the Iceland 3D simulation is shown in Figure 7a for 13 km altitude. The results shown in this figure corresponds to a moment when the wave field is fully developed, just before wave breaking sets in. The simulation suggests that mountain waves are excited by all major mountain ridges (cf.

Figure 1) and that the waves are able to propagate into the lower stratosphere. According to this simulation, the stratospheric amplitudes along the flight track are largest close to the turbulence encounter, whereas the remainder of the flight track had comparatively low-amplitude wave fields.

The cross-section along the HALO flight track of the Iceland 3D simulation (Figure 7b) shows notable differences to the Iceland 2D simulation along the same cross-section (Figure 5). In contrast to the 2D simulation, where the wave field is dominated by three distinct sources of mountain waves, the cross-section through the 3D results reveals mountain wave activity even when there is no steep orography below. Additionally, we find waves with large horizontal wavelengths (25 and 55 km, from wavelet analysis, not shown) at around 65°N, which is significantly larger than the dominant scales of the orography directly below the flight track at this position (10 km, from wavelet analysis, not shown). Larger-scale mountains are found to the east and the west of the flight track, namely Hofsjökull and Langjökull (blue and green topography in Figure 7b). The differences between the Iceland 2D and the Iceland 3D simulations suggest that the prevailing wave pattern along the flight track in the Iceland 3D simulation is not generated by the orography directly underneath the flight track but by mountains in its vicinity. These larger-scale waves are able to propagate freely through the troposphere (Figure 6) and thus they dominate the wave field at flight level. Their sources are not located directly below the flight track and these waves propagate both horizontally and vertically.

At flight level, steep isentropes occur close to the position of the turbulence encounter, as shown in Figure 7b. There are regions of negative Brunt–Väisälä frequency between 12 and 14 km altitude, which generally explains the turbulence at flight level. One of those convectively unstable regions is located at 64.9°N, almost exactly at the position of the turbulence encounter. Additionally, a second region with steep isentropes at flight level is found at 65.25°N which closely coincides with the secondary EDR peak (Figure 2d) at 65.36°N.

4.3 | Double-mountain domain

In this section we present simulations with the simplified, double-mountain orography which is described in Section 3.1. Based on the results from the Iceland 3D simulation, this double-mountain set-up was developed to study the horizontal propagation and interaction of mountain waves under idealized conditions. Only the two largest mountains close to the turbulence encounter, Hofsjökull and Langjökull, are considered.

These two mountains are represented by smooth and analytically defined Witch-of-Agnesi functions (Equation (2)). Smaller-scale orography is neglected because the Iceland 2D simulations showed that short waves become evanescent in the troposphere and are, therefore, of minor importance at flight level. In addition to the simulation with the double-mountain topography, we performed two more simulations with only one mountain each. This approach allows us to distinguish the contributions of the individual waves from each mountain to the wave-breaking process from contributions arising from the superposition and interaction of waves excited by the double-mountain flow.

4.3.1 | Both mountains

For an overview over the temporal development of the wave field and the breaking region, Figure 8 shows the vertical wind at 13 km altitude after (a) $t = 1$ hr, (b) $t = 1.42$ hr and (c) $t = 2.5$ hr. The mountain \mathcal{M}_E excites a wave with parabola-shaped phase lines (Smith, 1980). Because the other mountain \mathcal{M}_W is not circular but elliptical, the phase lines are straighter at the vertex of the parabola. Both waves propagate laterally into the region between the two mountains. Figure 8b shows the first small-scale structures which arise in the simulation. We find bands of alternating positive and negative vertical wind, which are aligned roughly parallel to the main wind direction and occur in an altitude range of negative stability. The horizontal spacing between the bands of strong positive vertical wind is about 1.5 to 2 km. With a horizontal resolution of less than 400 m in this part of the domain, they are represented by 5 to 6 grid points. These coherent bands have a lifetime of roughly 10 min ($t = 1.3$ hr to $t = 1.45$ hr) before they break down into small-scale and unstructured vertical wind fluctuations. Over the course of the simulation, the region of small-scale w perturbation increases until the two breaking regions merge (Figure 8c). At this time, the horizontal extent of the turbulent region is 50 km, with the farthest downstream extent between the two mountains.

The coherent structures from panel Figure 8b are analyzed in more detail in Figure 9. For this analysis, the flow field is interpolated onto the line connecting the two red dots in the inset of Figure 8b. The coordinate system is then rotated by 43.5° so that \tilde{u} is parallel and \tilde{v} is perpendicular to this cross-section. The y -component of the vorticity vector in the rotated coordinate system, $\tilde{\xi}_y = (\partial\tilde{u}/\partial z) - (\partial\tilde{w}/\partial x)$ (parallel to the band structures) is shown in Figure 9. We find horizontally aligned regions of enhanced vorticity with alternating signs. As the regions with enhanced vorticity extend downstream, these vorticity perturbations can be interpreted as horizontal vortex

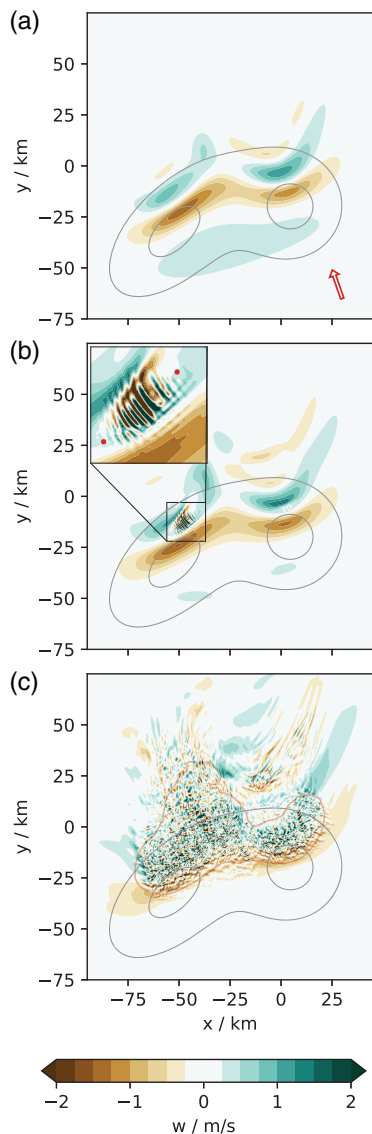


FIGURE 8 Vertical wind of the double mountain simulation in 13 km altitude at (a) $t = 1$ hr, (b) $t = 1.38$ hr and (c) $t = 2.5$ hr. Grey contours indicate 800 and 1,200 m elevation levels from the double-mountain topography. The arrow in (a) indicates the direction of the environmental wind in 13 km altitude. The red contour line in (c) delimits the area with $w_{\text{VAR}} = 0.5 \text{ m}^2/\text{s}^2$

tubes. A brief discussion of these vortex tubes follows in Section 5.

The breaking region extends vertically from 10 to 14.5 km altitude, as inferred from an analysis of the gravity wave drag (GWD). The GWD per unit mass is the density-normalized divergence of the vertical flux of horizontal momentum MF

$$\text{GWD}_{x,y} = -\frac{1}{\rho_e} \frac{\partial \text{MF}_{x,y}}{\partial z}. \quad (6)$$

The zonal and meridional components of the momentum flux are calculated as $\text{MF}_x = \rho_e \overline{u'w'}$ and $\text{MF}_y = \rho_e \overline{v'w'}$,

respectively. The overbar denotes horizontal averaging, with the averaging domain being the whole simulation domain excluding the sponge layers. Figure 10 depicts MF_y and GWD_y averaged over the time span between $t = 1.5$ hr (after the onset of wave breaking) and $t = 3.0$ hr. Enhanced negative GWD is found in the altitude range between 10 and 14.5 km, with a minimum of $-1.3 \text{ m}\cdot\text{s}^{-1}\cdot\text{hr}^{-1}$ at 13 km altitude.

A direct comparison of the aircraft *in situ* measurements and the simulation is shown in Figure 11. For this comparison, the simulation results are interpolated onto the flight path and, additionally, 400 m below the actually flown altitude. We show the lower altitude because, at the position of the turbulence encounter, the jet streak was at 10.2 km altitude according to ECMWF operational analysis. However, at the upstream point where the environmental profiles are extracted, the jet streak is 400 m lower. Therefore, to make the comparison at the correct altitude relative to the jet streak height, the comparison is also performed 400 m below the actual flight level. The comparison between observations and simulation is only meaningful in the vicinity of the two mountains (i.e. close to 65°N), because we have approximated the orography only in this region. Therefore, we do not expect to reproduce any wave signatures elsewhere along the path.

The observed decrease in the meridional wind v close to 65°N is reproduced in the simulations (Figure 11a, b). The comparison on the two different altitudes suggest that the horizontal position of the strong decrease in v depends on the altitude on which the comparison is performed (a versus b). Here, the lower altitude (b) shows better agreement. The magnitude of the decrease, which corresponds to the amplitude v' , shows reasonable agreement with the observations. The peak-to-peak amplitude is $19 \text{ m}\cdot\text{s}^{-1}$ in the simulation and $23 \text{ m}\cdot\text{s}^{-1}$ in the observations. The simulation and the observations both exhibit small-scale vertical wind fluctuations close to 65°N (Figure 11c, d), which is the region of strongest turbulence. In the simulation the vertical wind amplitudes along the HALO flight path are underestimated relative to the observations. The peak amplitude in the *in situ* observations is $6.3 \text{ m}\cdot\text{s}^{-1}$, whereas it is $4.6 \text{ m}\cdot\text{s}^{-1}$ in the simulation on the lower altitude (Figure 11d). For the zonal wind component, the agreement between observation and simulation is weak (Figure 11e, f). Both panels show a gradual decrease of u close to 65°N . The magnitude of the decrease is comparable to the observations, but the lateral position, absolute values and horizontal extent of the minimum do not agree. The large-scale peak in potential temperature close to 65°N is well reproduced in the simulation (Figure 11g, h). The peak-to-peak amplitude is 13.0 K in the observations and 12.5 K in the simulation. As for the comparison of v , the lower altitude (Figure 11h) shows better agreement in

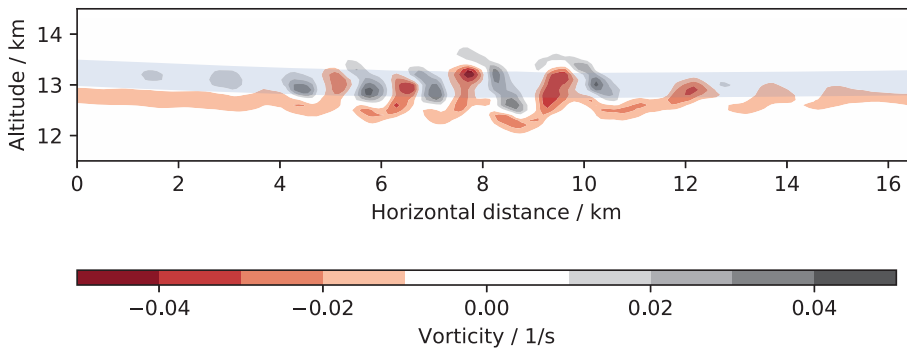


FIGURE 9 Vorticity ξ_y along cross-section between the two red dots in Figure 8b at $t = 1.38$ hr. The blue shaded region indicates where N^2 is negative prior to the development of the vortex tubes ($t = 1.3$ hr)

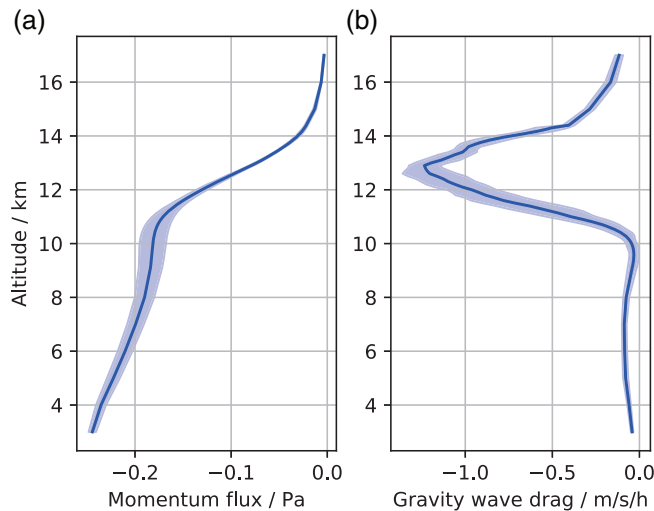


FIGURE 10 (a) Momentum flux MF_y and (b) gravity wave drag GWD_y averaged over the time span between $t = 1.5$ hr (after onset of wave breaking) and $t = 3.0$ hr. The shaded area denotes the standard deviation as a measure of the variability over the averaging period

terms of the horizontal position of the peak. The simulation generally shows a lower potential temperature, which is partly due to the lower altitude on which the comparison is performed.

4.3.2 | Superposition of individual mountains

To quantify the contributions of the individual mountain waves to the wave breaking, two further simulations are presented: one with only the western mountain \mathcal{M}_W and one with only the eastern mountain \mathcal{M}_E . Except the orography, all other parameters (such as environmental profiles, horizontal grid stretching and time-step) are kept unchanged. A linear superposition of the results of both simulations is calculated by adding the perturbations generated by each mountain to the environmental profiles, that is, $\theta_{\mathcal{M}_{W+E}} = \theta_e + \theta'_{\mathcal{M}_W} + \theta'_{\mathcal{M}_E}$ or $w_{\mathcal{M}_{W+E}} = w_{\mathcal{M}_W} + w_{\mathcal{M}_E}$,

since w_e is zero. This linear superposition is then compared to the model run described in Section 4.3.1. With that method, any difference between the two wave fields can be attributed to effects resulting from the presence and interference of the two waves. The simulation with the double-mountain orography is referred to as S_{WE} , whereas the linear superposition is referred to as S_{W+E} . The following analysis focuses on wave instability and breaking in the whole region between the two mountains.

Up to a simulation time of ~ 0.75 hr, the wave fields in S_{WE} and S_{W+E} are very similar. Differences between S_{WE} and S_{W+E} arise after wave breaking sets in, which is shown in Figure 12 for $t = 2$ hr. In S_{W+E} , small-scale fluctuations in the vertical wind occur slightly downstream of the two mountain peaks (top row). Even though these fluctuations develop at similar positions and with similar amplitudes in S_{WE} , the largest amplitudes in S_{WE} occur downstream and between the two mountains (bottom row). Here, fluctuations of $10 \text{ m}\cdot\text{s}^{-1}$ or more develop. This region of strong vertical wind fluctuations is absent in S_{W+E} .

A quantitative analysis of the magnitude of small-scale fluctuations occurring between the two mountains is presented in Figure 13. For this analysis, the vertical wind variance w_{VAR} is calculated on horizontal cross-sections of $r_{lim} = 10$ km radius which are centred around $x_c = -45$ km and $y_c = 10$ km, a point in the region with intense vertical wind fluctuations in S_{WE} . These cross-sections are indicated by the red circles in Figure 12.

Figure 13a, b show the vertical wind variance as a function of altitude. The largest values occur in the altitude range between 10 and 13 km. The vertical extent of the altitude range with enhanced w_{VAR} in S_{WE} is roughly twice as large as in S_{W+E} . In addition, the vertical wind variance in S_{WE} is almost a factor of 5 larger than in S_{W+E} at $t = 2$ hr. The difference decreases over time to a factor of 2 at $t = 3$ hr.

The temporal evolution of w_{VAR} is shown in Figure 13c, d for the altitudes of 12 and 10.7 km. The 12 km altitude lies within the maximum of w_{VAR} from S_{WE} and S_{W+E} , whereas the 10.7 km altitude falls into a local w_{VAR} minimum of S_{W+E} . At 12 km altitude

FIGURE 11 Comparison of HALO *insitu* measurements (grey curves) with numerical simulations (colored curves) from the double-mountain simulation at (a, c, e, g) 13.8 km altitude and (b, d, f, h) 13.4 km altitude. (a, b) show meridional wind, (c, d) vertical wind, (e, f) zonal wind and (g, h) potential temperature at $t = 3.0$ hr. The shaded region indicates the variability (minimum and maximum values) within a 2 km wide corridor between $t = 2.75$ hr to $t = 3.0$ hr

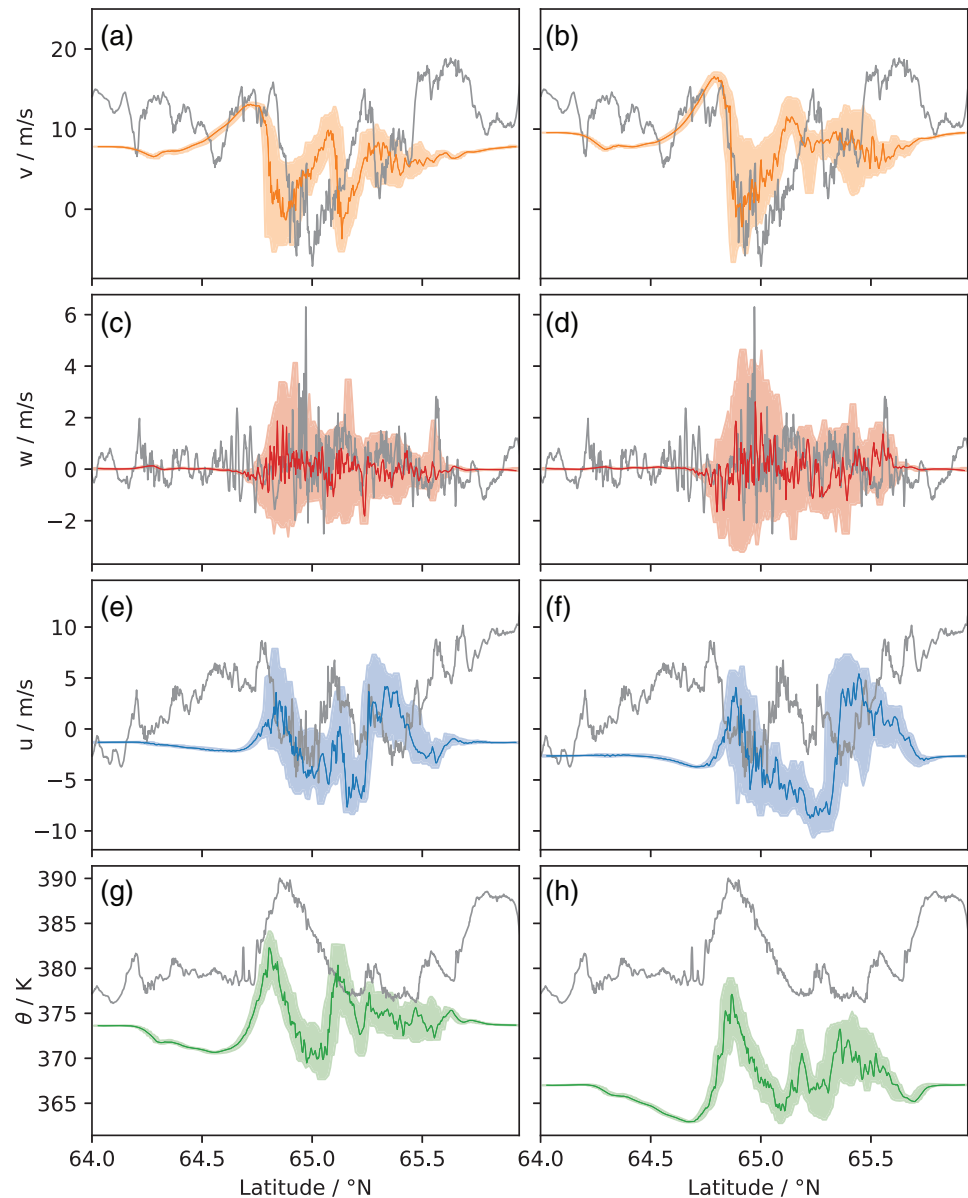


(Figure 13c) the vertical wind variance increases abruptly in the double-mountain simulation S_{WE} at $t = 1.5$ hr (shortly after convective instabilities appear at $t = 1.42$ hr; Figure 8), reaches its peak intensity at $t = 2$ hr, and then slowly decays. The vertical wind variance in the superposition (dashed line) gradually increases up to $t = 2.4$ hr and then stays roughly constant. At 10.7 km altitude (Figure 13d), w_{VAR} stays low over the whole course of the S_{W+E} simulation, whereas w_{VAR} values larger than in Figure 13c are reached in S_{WE} . Note that these results critically depend on the region chosen for the calculation of w_{VAR} . The region indicated by the red circle in Figure 12 is chosen to demonstrate how wave interference can locally intensify the vertical wind variance. The intensification is less prominent for other regions.

The intense small-scale vertical wind fluctuation downstream and between the two mountains can be explained by the superposition of the destabilizing phase of the two mountain waves. In the following analysis, we focus on the vertical gradients of potential temperature as a measure of static stability. In S_{W+E} , the potential temperature is written as

$$\theta = \theta_e + \theta'_{M_w} + \theta'_{M_e}, \quad (7)$$

which is the sum of ambient potential temperature θ_e and the perturbations θ' induced by the two mountains individually. Likewise, the potential temperature gradient has three contributions:

$$\frac{\partial}{\partial z} \theta = \frac{\partial}{\partial z} \theta_e + \frac{\partial}{\partial z} \theta'_{M_w} + \frac{\partial}{\partial z} \theta'_{M_e}. \quad (8)$$

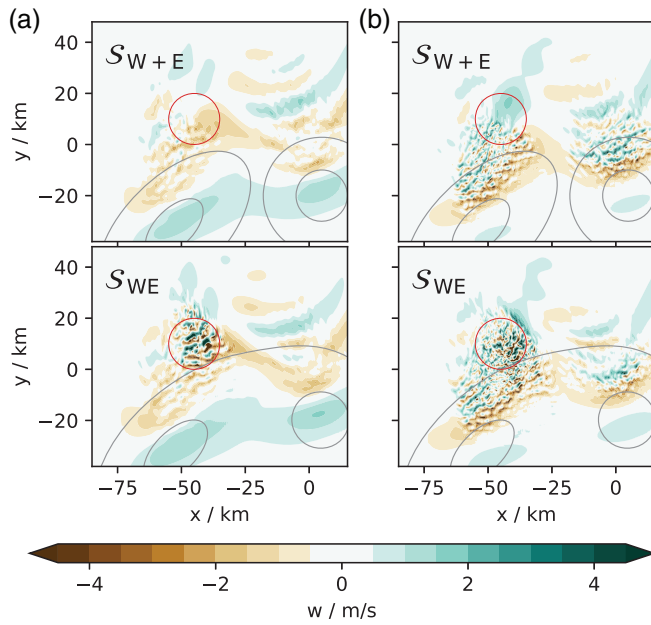


FIGURE 12 Vertical wind from (a, b) the superposition of simulations with individual mountains (S_{W+E}) and (c, d) the simulation with the double-mountain topography (S_{WE}). (a, c) are at 10.7 km and (b, d) at 12 km altitude at $t = 2$ hr. Black contours indicate 800 and 1,200 m elevation levels from (a, b) S_W and S_E and (c, d) from S_{WE} . The red circle denotes the region used for calculating w_{VAR}

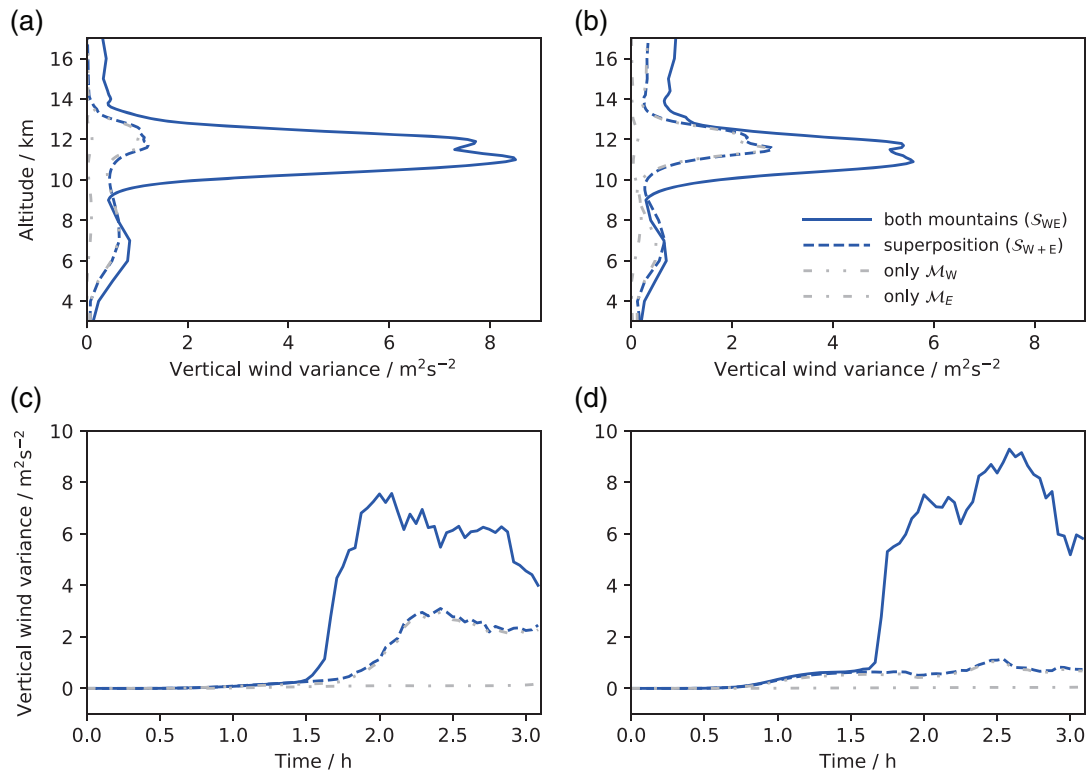


FIGURE 13 Vertical wind variance calculated on areas of 10 km radius centred on $x = -45$ km and $y = 10$ km (red circle in Figure 12). (a, b) show the vertical wind variance as a function of altitude at (a) $t = 2$ hr and (b) $t = 3$ hr. (c, d) show the time evolution of the vertical wind variance at (c) 12 km and (d) 10.7 km altitude. The vertical wind variance from the double-mountain simulation (S_{WE}) is drawn as a solid line, and that from the superposition of the two mountains (S_{W+E}) as a dashed line. The dash-dotted and dash-dot-dotted lines are the vertical wind variances from the simulations with only mountain M_E and only M_W , respectively

The gradient of θ_e is always positive, whereas the sign of the other two terms depends on the phase of the wave.

Figure 14 shows the different contributions to $\partial\theta/\partial z$. The shaded regions indicate the area where the wave's

perturbations destabilize the background, i.e. where $\partial\theta'_{M_W}/\partial z < 0$ (blue) and $\partial\theta'_{M_E}/\partial z < 0$ (green). These low-stability bands each have parabola shapes and lead to a checkerboard pattern in their superposition. The

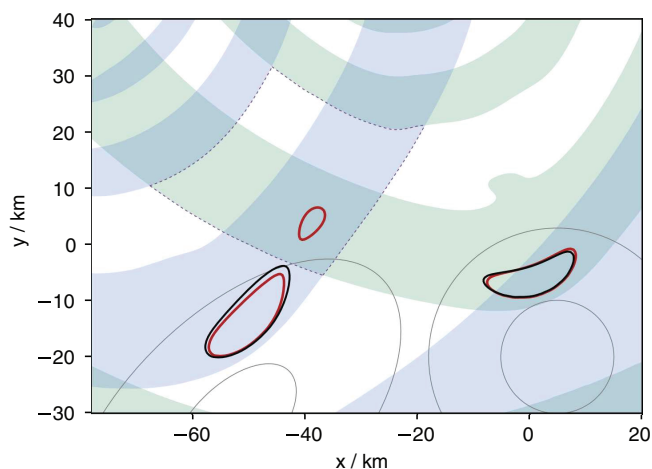


FIGURE 14 Contributions to atmospheric static stability from the individual mountain waves. Shaded regions indicate where the wave perturbations lead to a decrease of static stability. Black contours enclose area of negative total static stability caused by the individual mountain waves. Red contours enclose area of negative static stability in the linear superposition of the two waves. See text for further details. The cross-section is taken at 13 km altitude at $t = 1.25$ hr. Grey contours indicate 800 and 1,200 m elevation levels from S_W and S_E . The dotted line encloses an area which contains a complete wavelength of each mountain wave.

regions where both waves destabilize the background are coloured in a darker (turquoise) shade. The regions where both waves stabilize the already stable background are coloured white. The black contour lines denote where $\partial(\theta_e + \theta'_{M_W})/\partial z = 0$ and $\partial(\theta_e + \theta'_{M_E})/\partial z = 0$, i.e. where the amplitude of the individual mountain wave is large enough to overcome the background stability and initiate convective instabilities. This happens close to the mountain peaks. The red contour line indicates where $\partial(\theta_e + \theta'_{M_W} + \theta'_{M_E})/\partial z = 0$, i.e. it shows where convective instabilities will occur if both waves are linearly superposed. The figure shows that an additional region of negative total static stability occurs downstream and between the two mountains. Here, the individual temperature perturbations do not suffice for negative stability, but the linear superposition of both waves does. Not surprisingly, this is roughly the region where the large vertical wind amplitudes are found in S_{WE} (lower panels of Figure 12).

The temporal evolution of the turbulent region from S_{WE} , i.e. from the simulation including all nonlinearities and interactions between both mountain waves, is shown in Figure 15. For this analysis, the vertical wind variance is calculated with $r_{lim} = 7$ km at 13.4 km altitude. Choosing $r_{lim} = 7$ km is a compromise between a reasonable spatial resolution and including enough data points to obtain a meaningful variance. The vertical wind variance w_{VAR} is sampled every 3.5 km in x and y directions, so that we

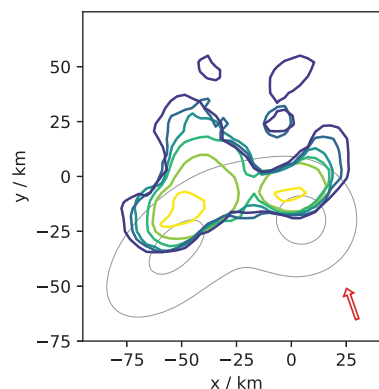


FIGURE 15 Temporal evolution of the region with enhanced vertical wind variance w_{VAR} at 13 km altitude. Bold contours delimit the area with $w_{VAR} > 0.5 \text{ m}^2/\text{s}^2$ for $t = 1.33$ hr (yellow) to $t = 3.0$ hr (dark blue) in steps of 0.33 hr (see text for further details). The arrow indicates the wind direction at this altitude and its length corresponds to horizontal wind speed multiplied by 0.33 hr. Thin contours indicate 800 and 1,200 m elevation levels

obtain partly overlapping regions on which the variance is calculated. The plot shows the outline of the region with $w_{VAR} > 0.5 \text{ m}^2 \cdot \text{s}^{-2}$ for different times. For comparison, the $w_{VAR} = 0.5 \text{ m}^2 \cdot \text{s}^{-2}$ contour line is also superimposed on Figure 8c.

In Figure 15, enhanced w_{VAR} occurs first close to the mountain tops. It then spreads downstream and also along the parabola-shaped phase lines (e.g. to the east of M_E and to the west of M_W). The farthest downstream extent of the turbulent region is between the two mountains and reaches roughly 50 km. A second turbulent region, which is detached from the main turbulent region, develops downstream of M_E . This turbulent patch is situated in a region where the wave excited by M_E destabilizes the background (green shaded region in Figure 14 at $x = 0$ and $y = 25$ km). Directly downstream of the mountain peaks, the contour lines delimiting the turbulent region do not develop over time, whereas the turbulent region does expand between the two mountains.

5 | DISCUSSION

The waves excited in the Iceland 2D simulations break in the altitude range between 13 and 15 km (Figure 5) which includes the flight level of HALO (13.8 km). The 2D simulations can therefore explain turbulence caused by mountain wave breaking at flight level. However, the horizontal position of the turbulence encounter is not correctly reproduced by the 2D simulation: strongest turbulence would be expected in region C of the Iceland 2D simulation because the largest vertical wind amplitudes and the largest horizontal extent of a negative stability region

occurs in region C. However, region C is approximately 100 km downstream of the observed position of strongest turbulence. According to the 2D simulations, only turbulence advected from region B, one of the weaker breaking regions, could be expected at the position of the observed strong turbulence. Therefore the 2D simulations fail to reproduce the observations, which show a localized peak in turbulence intensity slightly downstream of region B and only light turbulence or less in region C.

The 2D simulations in the study of Bramberger *et al.* (2020) are based on the same upstream environmental profiles but utilize the IFS orography consisting of a single mountain peak of about 50 km width on top of a plateau, missing all the small-scale mountain peaks in the centre of the Iceland 2D domain of this study (Figure 3a of this study and figure 4 of Bramberger *et al.* (2020)). There, the breaking region in the lower stratosphere extends from 64.7°N, the location of the mountain peak, northwards to 65°N, similarly to region B in this study. Thus, using a finer resolved topography does not lead to an improved representation of the turbulence location, which invalidates option 3 from the possible explanations stated in the Introduction.

The discrepancy of the turbulence position in the observation and the simulation is resolved in the Iceland 3D simulation. The horizontal cross-section of w in Figure 7a in conjunction with the topography in Figure 1 shows that the wave field close to the turbulence encounter is dominated by waves excited by the two mountains which are located to the east and west of the flight track. This is also demonstrated by the comparison of Figures 5 and 7b, which both show cross-sections along the HALO flight track, but from the 2D and 3D simulation, respectively. The most striking difference is that the tropospheric wave field in the 3D simulation is not dominated by three distinct sources of mountain waves as in the 2D simulation (regions A,B,C), but that there are w perturbations even when there is no steep topography below. This emphasizes the importance of the lateral propagation of mountain waves. The prevailing wave pattern at the turbulence encounter is thus not determined by the orography directly beneath the flight track, but by the mountains in the vicinity. The two dominating mountains in the vicinity (Hofsjökull and Langjökull) are higher and wider than the small mountain peaks in region B of the 2D topography (cf. black and color shaded topography in Figure 7b). Therefore, they are able to excite large-scale hydrostatic mountain waves which do not encounter an evanescent region, which leads to large-amplitude waves in the lower stratosphere and subsequent wave breaking.

From the horizontal cross-section in Figure 7a, we additionally infer that waves excited further upstream have

only a minimal impact on the wave field close to the turbulence encounter. The amplitudes of waves generated by the mountains at the southern coast of Iceland ($x = -25$ km and $y = -150$ km) strongly decrease downstream towards the turbulence encounter and are thus not expected to play a dominant role. These results from the Iceland 2D and 3D simulations are the motivation for simplifying the orography locally around the turbulence encounter, i.e. for the simulations with the idealized double-mountain orography.

Besides the orography simplification and the horizontally homogeneous background profiles, employing a free-slip lower boundary condition is a further major simplification. It was shown in several numerical experiments that increasing surface friction reduces the amplitudes of the excited gravity waves (e.g., Georgelin *et al.*, 1994; Ólafsson and Bougeault, 1997; Leutbecher and Volkert, 2000). Additionally, a fully developed boundary layer will modify the effective terrain shape (Peng and Thompson, 2003). Both aspects limit the comparability of the simulations to the *in situ* observations in terms of absolute wave amplitudes. However, as the main focus of this study is the horizontal dispersion and interference of two mountain waves with the subsequent wave breaking – and not the excitation of the waves itself – we chose to increase the grid point density at the centre of the domain, where the strong turbulence was observed, instead of close to the ground to resolve the boundary layer. Nevertheless, these restrictions should be kept in mind during the following comparison of *in situ* observations and simulation.

Despite the above-mentioned limitations, the double-mountain simulations reproduce the main characteristics of the *in situ* observations close to the turbulence encounter fairly well: they exhibit a strong decline in the horizontal wind, large amplitude vertical wind fluctuations and a peak in potential temperature. The comparison between observations and simulation shown in Figure 11 reveals a strong sensitivity of the position of these characteristics to the altitude on which the comparison is performed (left column versus right column). An upstream tilt of the wave's phase lines, as for example depicted for the Iceland 3D simulation in Figure 7b, is the cause for this shift in horizontal position with changing altitude. Better agreement is generally obtained for a comparison with model results at the lower altitude (13.4 km), which is expected to be the more realistic altitude relative to the jet streak height according to ECMWF (Section 4.3.1). This means that, for reproducing the correct horizontal position of the flow characteristics, the relative height above the jet streak is important in our case.

The peak amplitudes in the modelled vertical wind fluctuations directly along the HALO flight track

(Figure 11c, d) are lower than the observations. However, within a 2 km corridor around the flight track, vertical wind amplitudes up to $4.6 \text{ m} \cdot \text{s}^{-1}$ sporadically exist (shaded region). This suggests that, although the amplitudes at exactly the position of the flight track are smaller than the observations, the amplitudes in the vicinity reach comparable magnitudes. Taking the whole breaking region between the two mountains into account, the maximum vertical wind amplitudes reach $10 \text{ m} \cdot \text{s}^{-1}$ (Figure 12).

All simulations are initialized with horizontally homogeneous environmental profiles. These profiles capture the main characteristics of the vertical profile, such as tropopause and jet height, but horizontal gradients are not represented. As seen from the meteorological overview in Bramberger *et al.* (2020), the position of the jet core is slightly to the east of Iceland. The associated strong zonal gradient is thus not accounted for in the simulations. We suspect that the missing zonal gradient is the reason for the poor agreement between the *in situ* observations and the modelled zonal wind component (Figure 11c). Over the course of the flight leg, u changes by $\sim 20 \text{ m} \cdot \text{s}^{-1}$ (Figure 2). The large-scale change in v is only $\sim 5 \text{ m} \cdot \text{s}^{-1}$ and thus presumably has a smaller influence than the large-scale gradient of u .

In the double-mountain simulation, wave breaking is initiated by convective instabilities which appear slightly downstream of the mountain peaks. Horizontal vortex tubes develop as a result of overturning isentropes. These vortex tubes are aligned almost parallel to the mean flow and generate strong up- and downdraughts (Figure 8b). The vortex tubes appear at almost the smallest resolvable scales, which possibly affects the amplitude of the strong up- and downdraughts. Nevertheless, the generation of vortex tubes is a robust result, as they appear above both mountain peaks despite the mountains' different heights and aspect ratios $s_{x,i}/s_{y,i}$. Horizontal vortex tubes associated with convective instabilities have been recognized and studied in detail in numerous numerical studies of breaking gravity waves (e.g., Andreassen *et al.*, 1994; Fritts *et al.*, 1994; Isler *et al.*, 1994; Winters and D'Asaro, 1994; Fritts *et al.*, 1996; Afanasyev and Peltier, 1998; Andreassen *et al.*, 1998; Dörnbrack, 1998). As shown by Clark *et al.* (2000), horizontal vortex tubes can pose a serious risk for aircraft, although the vortex tubes in that study were not generated by breaking mountain waves but by thermal gradients associated with intense jet stream undulations.

Small-scale fluctuations between the two mountains are facilitated by the interference of the two waves excited by \mathcal{M}_W and \mathcal{M}_E . As demonstrated in Figure 14, negative total stability is obtained by the individual waves only close to the mountain peaks (black contour). The region of total

negative stability is limited to the vicinity of the mountain peaks because the wave's amplitude diminishes with increasing distance from the mountain peak (Smith, 1980). However, between the two mountains, the perturbations from both mountains waves jointly destabilize the background. This leads to an additional region of total negative stability between the two mountains (additional red contour in Figure 14). Thus, the individual temperature perturbations do not suffice for negative total stability, but the linear superposition of both waves does. This demonstrates that wave interference leads to an additional wave breaking region in our simulation, which is absent if we analyze the mountain waves individually.

In this framework of linear superposition, wave interference does not only create regions of enhanced instability, but also regions of enhanced stability. When considering an area which contains a complete wavelength of both waves (dashed line in Figure 14), three different subregions can be identified: A subregion where (1) both waves stabilize the background (white subregion in Figure 14), (2) both waves destabilize the background (darker turquoise shade) and (3) one wave stabilizes and the other destabilizes the background (light green and light blue subregions). For equal-amplitude waves, the destructive interference in the latter region would lead to a negligible (local) wave amplitude and would suppress wave overturning. From the three regions, the possibility for wave overturning is limited to subregion (2). If we assume that the intensity of turbulence generated by a breaking gravity wave increases with wave energy, doubling of the wave amplitude in subregion (2) would lead to a quadrupling of the local wave energy. In this sense wave interference can lead to an increase of turbulence intensity by confining wave overturning to one of the subregions. In the specific case analyzed in this study, the situation is slightly more complicated since the wave amplitudes are not equal and decrease along the wave's phase lines. Nevertheless, we believe this conceptual picture helps explaining the strong increase of the vertical wind variance of S_{WE} shown in Figure 13. For this analysis the vertical wind variance was calculated mostly over a region of enhanced instability in order to show how turbulence intensity can be locally enhanced by wave interference.

It is worth noting here that, until shortly before wave breaking sets in, the difference between S_{WE} and S_{W+E} is insignificant, which means that the wave field of S_{WE} is very well approximated by the linear superposition of the individual mountain waves. The subsequent deviation from linearity has two reasons:

- (1) Wave-wave interaction leads to slightly larger amplitudes in S_{WE} directly before wave overturning.

- (2) The transition to turbulence is controlled by a threshold condition on the wave amplitude, which is reached at an earlier time and in a larger domain in S_{WE} than in S_{W+E} .

Due to this ‘threshold nature’, the turbulent flow in Figure 12 shows large deviations from the linear superposition.

To assess whether advection was the cause for the downstream position of the observed turbulence, we perform a simple estimate of the turbulence decay time τ based on the turbulent kinetic energy (TKE) and the energy dissipation rate ε . Assuming for the moment that there was no local turbulence source, the turbulence lifetime could be estimated via $\tau = TKE/\varepsilon$. This estimate is based on the energy cascade in the inertial subrange, in which the energy flux through the different scales is given by ε (e.g., Tennekes and Lumley, 1972, chapter 8.4). In the study of Bramberger *et al.* (2020), TKE is derived from high-resolution *in situ* observations along the flight track. Maximum TKE values ($TKE_{\max} = 10 \text{ m}^2 \cdot \text{s}^{-2}$) are obtained at the position of the EDR peak. From ε_{\max} and TKE_{\max} , we obtain $\tau = 2.8 \text{ min}$. This means that, without a continuous energy input, turbulence of the observed intensity would be dissipated after 2.8 min, or after being advected 2 km. Thus, any turbulence generated over a finite time by an upstream source and then advected seems very unlikely.

Nevertheless, advection could still play a role for the formation of the extended turbulent region between the two mountains. To what extent the small-scale wind fluctuations are possibly advected with the background wind can be inferred from Figure 15. The red arrow in that figure shows the orientation and strength of the environmental wind. Its length indicates the distance any disturbance is advected by the environmental wind within 20 min, which is the temporal spacing of the contour lines. The expansion of the turbulent region between the mountains progresses with roughly half the background wind speed. In contrast to that, the turbulent regions directly downstream of the mountain peaks expand laterally along the wave’s phase lines, which cannot be explained by advection. Instead, the wave’s amplitude increases over time, which leads to amplitudes large enough for overturning farther and farther away from the mountain peaks. The observation that there is a sharp dividing line behind \mathcal{M}_E , which does not move with the advection velocity, suggests that advection cannot generally be the dominant reason for the large downstream extent between the two mountains. It seems more likely that the increasing wave amplitudes and their interference lead to further breaking regions also between the two mountains. This is supported by the checkerboard pattern in Figure 14, which shows several regions of concurrent destabilization.

The turbulence experienced by HALO occurred above the jet streak in a region of decreasing horizontal wind speeds. This raises the question of which role shear played for the generation of turbulence. The initial shear provided by the large-scale flow is not large enough to support dynamic instabilities. In the environmental profiles, the gradient Richardson number $Ri = N^2 / \{(\partial u / \partial z)^2 + (\partial v / \partial z)^2\}$ is larger than 6 everywhere. However, as the horizontal wind speed decreases with altitude between 10 and 15 km altitude, the nonlinearity ratios v'/v_e and u'/u_e increase for a given perturbation. In the case of mountain waves with phase speed zero, nonlinearity ratios larger than ~ 1 are indicative of negative gradients of potential temperature (e.g., Orlanski and Bryan, 1969; Walterscheid and Schubert, 1990), i.e. of convective instabilities. Thus, the strong shear zone above the jet streak facilitated convective instabilities in concert with additional perturbations due to mountain waves, but the background shear was in our simulations not large enough to form dynamic instabilities.

The vertical wind variance shown in Figure 13 can be interpreted as a measure of turbulence intensity. From the analysis of the vertical wind variance the contribution of wave interference to the turbulence intensity can be inferred. Because the contribution of w_{VAR} from the mountain wave generated by \mathcal{M}_E is negligible, the large difference between S_{WE} and S_{W+E} must be due to the interference of the two waves. Thus, wave interference leads to notably stronger turbulence in the region between the two mountains and is the deciding factor that determines whether there is turbulence or not. This applies in particular to the altitude of 10.7 km, which falls into the range of typical cruising altitudes of commercial aircraft.

6 | SUMMARY AND CONCLUSION

Based on the simulations and analyzes presented in Section 4, we conclude that mountain wave breaking is the primary cause for the turbulence encountered by HALO over central Iceland. The ambient conditions favour the excitation of mountain waves. These mountain waves are able to propagate through the troposphere and become convectively unstable in an altitude range around flight level. Close agreement in the horizontal position of convectively unstable regions in the simulations and the observed turbulence is obtained when the waves are allowed to propagate three-dimensionally. The simulations with the idealized double-mountain orography reproduces the large-scale gradients of v and θ very well, both in position and magnitude. Additionally, the large-amplitude small-scale vertical wind fluctuations

occur in the double-mountain simulation at the position of the turbulence encounter. Therefore, the two isolated hills to the east and west of the flight track (Hofsjökull and Longjökull) can be considered as the main source of the waves relevant for the turbulence event.

In the Introduction we raised the question why the turbulence was observed downstream of the two mountain peaks. The simulations support the proposed hypothesis that waves excited by mountains in the vicinity of the flight track break downstream of and between the mountains. However, the analysis showed that one essential mechanism leading to wave breaking in this region is the superposition of the two mountain waves. Individually, the waves do generate turbulence in this region, but with wave interference the turbulence strength increases by a factor of 5.

Concerning the other three proposed mechanisms ((1) shear, (2) advection and (3) unresolved orography), we conclude that none of them is the dominant source of the observed turbulence:

1. HALO was flying in a region of strong vertical shear above the jet streak. Based on the environmental profiles derived from ECMWF operational analysis, the Richardson number was 6 or larger. Thus, shear alone was not large enough to generate dynamic instabilities. Nevertheless, the negative shear above the jet streak contributed to wave breaking by reducing the vertical wavelength and facilitating wave overturning. Thus, only the combined effect of shear and mountain wave excitation led to the generation of turbulence.
2. The downwind position of the observed turbulence is unlikely caused by advection. The turbulence decay time is only a few minutes, which means that turbulent fluctuations are viscously dissipated within a few minutes. If the observed turbulence were to be generated by wave breaking directly above the mountain peaks, the turbulence would have had to survive ~ 15 decay times. As this is unrealistic, we conclude that the spatial distribution of observed turbulence roughly reflects the spatial distribution of the turbulence source.
3. Employing finer-resolved orography for the 2D simulations does not lead to any improvement in modelling the correct position of the mountain wave breaking. Instead of improving the simulations, the finer-resolved orography yields waves which become partly evanescent in the troposphere. These waves are strongly damped and therefore less likely to generate turbulence in the lower stratosphere. We conclude that increasing the resolution of the orography is not beneficial in this case. Indeed, the double-mountain orography in this study exploited this result by

removing all small-scale features and approximating the orography by two idealized mountains.

Finally, we conclude that wave interference can locally facilitate wave breaking and can notably contribute to the intensity of mountain wave turbulence. Furthermore, this study shows that the three-dimensional propagation of mountain waves can be important when interpreting flight level data over rough terrain with isolated mountain peaks. In such cases the orography directly beneath the flight track is not necessarily decisive for the wave field measured above.

ACKNOWLEDGEMENTS

This research was partly funded by the Deutsche Forschungsgemeinschaft (DFG) via the project MS-GWaves (GW-TP/DO 1020/9-1, PACOG/RA 1400/6-1). Access to ECMWF data was granted through the special project "Deep Vertical Propagation of Internal Gravity Waves".

ORCID

Henrike Wilms  <https://orcid.org/0000-0001-9428-1736>

REFERENCES

- Afanasyev, Y.D. and Peltier, W.R. (1998) The three-dimensionalization of stratified flow over two-dimensional topography. *Journal of the Atmospheric Sciences*, 55, 19–39. [https://doi.org/10.1175/1520-0469\(1998\)055<0019:ttosdf>2.0.co;2](https://doi.org/10.1175/1520-0469(1998)055<0019:ttosdf>2.0.co;2)
- Amante, C. and Eakins, B.W. (2009) *ETOPO1 1 Arc-Minute Global Relief Model: Procedures, Data Sources and Analysis*. NOAA Technical Memorandum NESDIS NGDC-24, National Geophysical Data Center, Boulder, CO.
- Andreassen, Ø., Hvidsten, P.Ø., Fritts, D.C. and Arendt, S. (1998) Vorticity dynamics in a breaking internal gravity wave. Part 1. Initial instability evolution. *Journal of Fluid Mechanics*, 367, 27–46. <https://doi.org/10.1017/s0022112098001645>
- Andreassen, Ø., Wasberg, C.E., Fritts, D.C. and Isler, J.R. (1994) Gravity wave breaking in two and three dimensions: 1. Model description and comparison of two-dimensional evolutions. *Journal of Geophysical Research*, 99, 8095. <https://doi.org/10.1029/93jd03435>
- Bacmeister, J.T. and Schoeberl, M.R. (1989) Breakdown of vertically propagating two-dimensional gravity waves forced by orography. *Journal of the Atmospheric Sciences*, 46, 2109–2134. [https://doi.org/10.1175/1520-0469\(1989\)046<2109:bovptd>2.0.co;2](https://doi.org/10.1175/1520-0469(1989)046<2109:bovptd>2.0.co;2)
- Bramberger, M., Dörnbrack, A., Wilms, H., Gemsa, S., Raynor, K. and Sharman, R. (2018) Vertically propagating mountain waves – a hazard for high-flying aircraft?. *Journal of Applied Meteorology and Climatology*, 57, 1957–1975. <https://doi.org/10.1175/jamc-d-17-0340.1>
- Bramberger, M., Dörnbrack, A., Wilms, H. and Sharman, R. (2020) Mountain wave turbulence encounter of the research aircraft HALO above Iceland. *Journal of Applied Meteorology and Climatology*, 59, 567–588. <https://doi.org/10.1175/JAMC-D-19-0079.1>

- Clark, T.L. and Farley, R.D. (1984) Severe downslope windstorm calculations in two and three spatial dimensions using anelastic interactive grid nesting: a possible mechanism for gustiness. *Journal of the Atmospheric Sciences*, 41, 329–350. [https://doi.org/10.1175/1520-0469\(1984\)041<0329:sdwcit>2.0.co;2](https://doi.org/10.1175/1520-0469(1984)041<0329:sdwcit>2.0.co;2)
- Clark, T.L., Hall, W.D., Kerr, R.M., Middleton, D., Radke, L., Ralph, F.M., Neiman, P.J. and Levinson, D. (2000) Origins of aircraft-damaging clear-air turbulence during the 9 December 1992 Colorado downslope windstorm: numerical simulations and comparison with observations. *Journal of the Atmospheric Sciences*, 57, 1105–1131. [https://doi.org/10.1175/1520-0469\(2000\)057<1105:oodaca>2.0.co;2](https://doi.org/10.1175/1520-0469(2000)057<1105:oodaca>2.0.co;2)
- Dörnbrack, A. (1998) Turbulent mixing by breaking gravity waves. *Journal of Fluid Dynamics*, 375, 113–141. <https://doi.org/10.1017/S0022112098002833>
- Doyle, J.D., Shapiro, M.A., Jiang, Q. and Bartels, D.L. (2005) Large-amplitude mountain wave breaking over Greenland. *Journal of the Atmospheric Sciences*, 62, 3106–3126. <https://doi.org/10.1175/jas3528.1>
- Doyle, J.D., Gaberšek, S., Jiang, Q., Bernardet, L., Brown, J.M., Dörnbrack, A., Filaus, E., Grubišić, V., Kirshbaum, D.J., Knoth, O., Koch, S., Schmidli, J., Stiperski, I., Vosper, S.B. and Zhong, S. (2011) An intercomparison of T-REX mountain-wave simulations and implications for mesoscale predictability. *Monthly Weather Review*, 139, 2811–2831. <https://doi.org/10.1175/mwr-d-10-05042.1>
- Fritts, D.C., Isler, J.R. and Andreassen, Ø. (1994) Gravity wave breaking in two and three dimensions: 2. Three-dimensional evolution and instability structure. *Journal of Geophysical Research; Atmospheres*, 99, 8109–8123. <https://doi.org/10.1029/93jd03436>
- Fritts, D.C., Garten, J.F. and Andreassen, Ø. (1996) Wave breaking and transition to turbulence in stratified shear flows. *Journal of the Atmospheric Sciences*, 53, 1057–1085. [https://doi.org/10.1175/1520-0469\(1996\)053<1057:WBATTT>2.0.CO;2](https://doi.org/10.1175/1520-0469(1996)053<1057:WBATTT>2.0.CO;2)
- Gal-Chen, T. and Somerville, R.C. (1975) On the use of a coordinate transformation for the solution of the Navier–Stokes equations. *Journal of Computational Physics*, 17, 209–228. [https://doi.org/10.1016/0021-9991\(75\)90037-6](https://doi.org/10.1016/0021-9991(75)90037-6)
- Georgelin, M., Richard, E., Petitdidier, M. and Druilhet, A. (1994) Impact of subgrid-scale orography parameterization on the simulation of orographic flows. *Monthly Weather Review*, 122, 1509–1522. [https://doi.org/10.1175/1520-0493\(1994\)122<1509:IOSSOP>2.0.CO;2](https://doi.org/10.1175/1520-0493(1994)122<1509:IOSSOP>2.0.CO;2)
- Grinstein, F.F., Margolin, L.G. and Rider, W.J. (Eds.) (2007) *Implicit Large-Eddy Simulation*. Cambridge University Press, Cambridge, UK.
- Grisogono, B., Pryor, S.C. and Keislar, R.E. (1993) Mountain wave drag over double bell-shaped orography. *Quarterly Journal of the Royal Meteorological Society*, 119, 199–206. <https://doi.org/10.1002/qj.49711950909>
- Grubišić, V. and Stiperski, I. (2009) Lee-wave resonances over double bell-shaped obstacles. *Journal of the Atmospheric Sciences*, 66, 1205–1228. <https://doi.org/10.1175/2008jas2885.1>
- Gyüre, B. and János, I.M. (2003) Stratified flow over asymmetric and double bell-shaped obstacles. *Dynamics of Atmospheres and Oceans*, 37, 155–170. [https://doi.org/10.1016/s0377-0265\(03\)00030-7](https://doi.org/10.1016/s0377-0265(03)00030-7)
- Isler, J.R., Fritts, D.C., Andreassen, Ø. and Wasberg, C.E. (1994) Gravity wave breaking in two and three dimensions: 3. Vortex breakdown and transition to isotropy. *Journal of Geophysical Research; Atmospheres*, 99, 8125–8137. <https://doi.org/10.1029/93JD03437>
- Jiang, Q. and Doyle, J.D. (2004) Gravity wave breaking over the central Alps: role of complex terrain. *Journal of the Atmospheric Sciences*, 61, 2249–2266. [https://doi.org/10.1175/1520-0469\(2004\)061<2249:gwbtc>2.0.co;2](https://doi.org/10.1175/1520-0469(2004)061<2249:gwbtc>2.0.co;2)
- Koch, S.E., Jamison, B.D., Lu C., Smith T.L., Tollerud E.I., Girz C., Wang N., Lane T.P., Shapiro M.A., Parrish D.D. and Cooper O.R. (2005) Turbulence and gravity waves within an upper-level front. *Journal of the Atmospheric Sciences*, 62, 3885–3908. <https://doi.org/10.1175/jas3574.1>
- Kühnlein, C., Smolarkiewicz, P.K. and Dörnbrack, A. (2012) Modelling atmospheric flows with adaptive moving meshes. *Journal of Computational Physics*, 231, 2741–2763. <https://doi.org/10.1016/j.jcp.2011.12.012>
- Kurowski, M.J., Wojcik, D.K., Ziemianski, M.Z., Rosa, B. and Piotrowski, Z.P. (2016) Convection-permitting regional weather modeling with COSMO-EULAG: compressible and anelastic solutions for a typical westerly flow over the alps. *Monthly Weather Review*, 144, 1961–1982. <https://doi.org/10.1175/mwr-d-15-0264.1>
- Lane, T.P., Doyle, J.D., Plougonven, R., Shapiro, M.A. and Sharman, R.D. (2004) Observations and numerical simulations of inertia gravity waves and shearing instabilities in the vicinity of a jet stream. *Journal of the Atmospheric Sciences*, 61, 2692–2706. <https://doi.org/10.1175/jas3305.1>
- Lane, T.P., Doyle, J.D., Sharman, R.D., Shapiro, M.A. and Watson, C.D. (2009) Statistics and dynamics of aircraft encounters of turbulence over Greenland. *Monthly Weather Review*, 137, 2687–2702. <https://doi.org/10.1175/2009mwr2878.1>
- Lee, Y., Muraki, D.J. and Alexander, D.E. (2006) A resonant instability of steady mountain waves. *Journal of Fluid Mechanics*, 568, 303–327. <https://doi.org/10.1017/S002211200600231X>
- Leutbecher, M. and Volkert, H. (2000) The propagation of mountain waves into the stratosphere: quantitative evaluation of three-dimensional simulations. *Journal of the Atmospheric Sciences*, 57, 3090–3108. [https://doi.org/10.1175/1520-0469\(2000\)057<3090:TPOMWI>2.0.CO;2](https://doi.org/10.1175/1520-0469(2000)057<3090:TPOMWI>2.0.CO;2)
- Lin, Y.-L. (2007) *Mesoscale Dynamics*. Cambridge University Press, Cambridge, UK.
- Lipps, F.B. and Hemler, R.S. (1982) A scale analysis of deep moist convection and some related numerical calculations. *Journal of the Atmospheric Sciences*, 39, 2192–2210. [https://doi.org/10.1175/1520-0469\(1982\)039<2192:asaadm>2.0.co;2](https://doi.org/10.1175/1520-0469(1982)039<2192:asaadm>2.0.co;2)
- Mayr, G.J. and Gohm, A. (2000) 2D airflow over a double bell-shaped mountain. *Meteorology and Atmospheric Physics*, 72, 13–27. <https://doi.org/10.1007/s007030050002>
- Ogura, Y. and Phillips, N.A. (1962) Scale analysis of deep and shallow convection in the atmosphere. *Journal of the Atmospheric Sciences*, 19, 173–179. [https://doi.org/10.1175/1520-0469\(1962\)019<0173:saodas>2.0.co;2](https://doi.org/10.1175/1520-0469(1962)019<0173:saodas>2.0.co;2)
- Ólafsson, H. and Ágústsson, H. (2009) Gravity wave breaking in easterly flow over Greenland and associated low-level barrier and reverse tip-jets. *Meteorology and Atmospheric Physics*, 104, 191–197. <https://doi.org/10.1007/s00703-009-0024-9>
- Ólafsson, H. and Bougeault, P. (1997) The effect of rotation and surface friction on orographic drag. *Journal of the Atmospheric Sciences*, 54, 193–210. [https://doi.org/10.1175/1520-0469\(1997\)054<0193:TEORAS>2.0.CO;2](https://doi.org/10.1175/1520-0469(1997)054<0193:TEORAS>2.0.CO;2)

- Orlanski, I. and Bryan, K. (1969) Formation of the thermocline step structure by large-amplitude internal gravity waves. *Journal of Geophysical Research*, 74, 6975–6983. <https://doi.org/10.1029/JC074i028p06975>
- Pavelin, E., Whiteway, J.A. and Vaughan, G. (2001) Observation of gravity wave generation and breaking in the lowermost stratosphere. *Journal of Geophysical Research: Atmospheres*, 106, 5173–5179. <https://doi.org/10.1029/2000jd900480>
- Pedersen, J.G., Ma, Y.-F., Grabowski, W.W. and Malinowski, S.P. (2018) Anisotropy of observed and simulated turbulence in marine stratocumulus. *Journal of Advances in Modeling Earth Systems*, 10, 500–515. <https://doi.org/10.1002/2017ms001140>
- Peng, M.S. and Thompson, W.T. (2003) Some aspects of the effect of surface friction on flows over mountains. *Quarterly Journal of the Royal Meteorological Society*, 129, 2527–2557. <https://doi.org/10.1256/qj.02.06>
- Prusa, J.M., Smolarkiewicz, P.K. and Garcia, R.R. (1996) Propagation and breaking at high altitudes of gravity waves excited by tropospheric forcing. *Journal of the Atmospheric Sciences*, 53, 2186–2216. [https://doi.org/10.1175/1520-0469\(1996\)053<2186:pabaha>2.0.co;2](https://doi.org/10.1175/1520-0469(1996)053<2186:pabaha>2.0.co;2)
- Prusa, J.M., Smolarkiewicz, P.K. and Wyszogrodzki, A.A. (2008) EULAG, a computational model for multiscale flows. *Computers and Fluids*, 37, 1193–1207. <https://doi.org/10.1016/j.compfluid.2007.12.001>
- Reuder, J., Ablinger, M., Ágústsson, H., Brisset, P., Brynjólfsson, S., Garhammer, M., Jóhannesson, T., Jonassen, M.O., K’uhnel, R., L’ammlein, S., de Lange, T.E., Lindenberg, C., Malardel, S., Mayer, S., M’uller, M., Ólafsson, H., R’ognvaldsson, Ó., Sch’aper, W., Spengler, T., Z’angl, G. and Egger, J. (2012) FLO-HOF 2007: an overview of the mesoscale meteorological field campaign at Hofsjökull, Central Iceland. *Meteorology and Atmospheric Physics*, 116, 1–13. <https://doi.org/10.1007/s00703-010-0118-4>
- Schäfler, A., Craig, G., Wernli, H., Arbogast, P., Doyle, J.D., McTaggart-Cowan, R., Methven, J., Rivière, G., Ament, F., Boettcher, M., Bramberger, M., Cazenave, Q., Cotton, R., Crewell, S., Delano’ e, J., D’ornbrack, A., Ehrlich, A., Ewald, F., Fix, A., Grams, C.M., Gray, S.L., Grob, H., Gross, S., Hagen, M., Harvey, B., Hirsch, L., Jacob, M., K’olling, T., Konow, H., Lemmerz, C., Lux, O., Magnusson, L., Mayer, B., Mech, M., Moore, R., Pelon, J., Quinting, J., Rahm, S., Rapp, M., Rautenhaus, M., Reitebuch, O., Reynolds, C.A., Sodemann, H., Spengler, T., Vaughan, G., Wendisch, M., Wirth, M., Witschas, B., Wolf, K. and Zinner, T. (2018) The North Atlantic waveguide and downstream impact experiment. *Bulletin of the American Meteorological Society*, 99, 1607–1637. <https://doi.org/10.1175/bams-d-17-0003.1>
- Schmid, H. and Dörnbrack, A. (1999) Simulation of breaking gravity waves during the south foehn of 7–13 January 1996. *Contributions to Atmospheric Physics*, 72, 287–301
- Sharman, R.D. and Wurtele, M.G. (2004) Three-dimensional structure of forced gravity waves and lee waves. *Journal of the Atmospheric Sciences*, 61, 664–681. [https://doi.org/10.1175/1520-0469\(2004\)061<0664:tsofgw>2.0.co;2](https://doi.org/10.1175/1520-0469(2004)061<0664:tsofgw>2.0.co;2)
- Sharman, R.D., Doyle, J.D. and Shapiro, M.A. (2012a) An investigation of a commercial aircraft encounter with severe clear-air turbulence over western Greenland. *Journal of Applied Meteorology and Climatology*, 51, 42–53. <https://doi.org/10.1175/jamc-d-11-044.1>
- Sharman, R.D., Trier, S.B., Lane, T.P. and Doyle, J.D. (2012b) Sources and dynamics of turbulence in the upper troposphere and lower stratosphere: a review. *Geophysical Research Letters*, 39(12). <https://doi.org/10.1029/2012GL051996>
- Sharman, R.D., Cornman, L.B., Meymaris, G., Pearson, J. and Farar, T. (2014) Description and derived climatologies of automated *in situ* eddy-dissipation-rate reports of atmospheric turbulence. *Journal of Applied Meteorology and Climatology*, 53, 1416–1432. <https://doi.org/10.1175/jamc-d-13-0329.1>
- Skamarock, W.C., Smolarkiewicz, P.K. and Klemp, J.B. (1997) Preconditioned conjugate-residual solvers for Helmholtz equations in non-hydrostatic models. *Monthly Weather Review*, 125, 587–599. [https://doi.org/10.1175/1520-0493\(1997\)125<0587:pcrsfh>2.0.co;2](https://doi.org/10.1175/1520-0493(1997)125<0587:pcrsfh>2.0.co;2)
- Smith, R.B. (1980) Linear theory of stratified hydrostatic flow past an isolated mountain. *Tellus*, 32, 348–364. <https://doi.org/10.1111/j.2153-3490.1980.tb00962.x>
- Smolarkiewicz, P.K. (2006) Multidimensional positive definite advection transport algorithm: an overview. *International Journal for Numerical Methods in Fluids*, 50, 1123–1144. <https://doi.org/10.1002/fld.1071>
- Smolarkiewicz, P.K. and Margolin, L.G. (1994) Variational solver for elliptic problems in atmospheric flows. *Applied Mathematics and Computation Science*, 4, 527–551
- Smolarkiewicz, P.K. and Margolin, L.G. (1997) On forward-in-time differencing for fluids: an Eulerian/semi-Lagrangian non-hydrostatic model for stratified flows. *Atmosphere–Ocean*, 35, 127–152. <https://doi.org/10.1080/07055900.1997.9687345>
- Smolarkiewicz, P.K. and Margolin, L.G. (1998) MPDATA: a finite-difference solver for geophysical flows. *Journal of Computational Physics*, 140, 459–480
- Sorbjan, Z. (1996) Numerical study of penetrative and “solid lid” non-penetrative convective boundary layers. *Journal of the Atmospheric Sciences*, 53, 101–112. [https://doi.org/10.1175/1520-0469\(1996\)053<0101:NSOPAL>2.0.CO;2](https://doi.org/10.1175/1520-0469(1996)053<0101:NSOPAL>2.0.CO;2)
- Stiperski, I. and Grubišić, V. (2011) Trapped lee wave interference in the presence of surface friction. *Journal of the Atmospheric Sciences*, 68, 918–936. <https://doi.org/10.1175/2010jas3495.1>
- Stiperski, I., Serafin, S., Paci, A., Ágústsson, H., Belleudy, A., Calmer, R., Horvath, K., Knigge, C., Sachsperger, J., Strauss, L. and Grubišić, V. (2017) Water tank experiments on stratified flow over double mountain-shaped obstacles at high Reynolds number. *Atmosphere*, 8, 13. <https://doi.org/10.3390/atmos8010013>
- Tennekes, H. and Lumley, J.L. (1972) *A First Course in Turbulence*. MIT Press, Cambridge, MA.
- Tvryanas, A.P. (2003) Epidemiology of turbulence-related injuries in airline cabin crew, 1992–2001. *Aviation Space and Environmental Medicine*, 74, 970–976
- Uhlenbrock, N.L., Bedka, K.M., Feltz, W.F. and Ackerman, S.A. (2007) Mountain wave signatures in MODIS 6.7 μm imagery and their relation to pilot reports of turbulence. *Weather and Forecasting*, 22, 662–670. <https://doi.org/10.1175/waf1007.1>
- van der Mescht, D. and Geldenhuys, M. (2019) Observations of mountain waves with interference generated by coastal mountains in South Africa. *Meteorological Applications*, 26, 409–415. <https://doi.org/10.1002/met.1771>
- Vosper, S.B. (1996) Gravity-wave drag on two mountains. *Quarterly Journal of the Royal Meteorological Society*, 122, 993–999. <https://doi.org/10.1002/qj.49712253211>

- Walterscheid, R.L. and Schubert, G. (1990) Nonlinear evolution of an upward propagating gravity wave: overturning, convection, transience and turbulence. *Journal of the Atmospheric Sciences*, 47, 101–125. [https://doi.org/10.1175/1520-0469\(1990\)047<0101:neoaup>2.0.co;2](https://doi.org/10.1175/1520-0469(1990)047<0101:neoaup>2.0.co;2)
- Wedi, N.P. and Smolarkiewicz, P.K. (2003) Extending Gal-Chen and Somerville terrain-following coordinate transformation on time-dependent curvilinear boundaries. *Journal of Computational Physics*, 193, 1–20. <https://doi.org/10.1016/j.jcp.2003.07.034>
- Winters, K.B. and D'Asaro, E.A. (1994) Three-dimensional wave instability near a critical level. *Journal of Fluid Mechanics*, 272, 255–284. <https://doi.org/10.1017/s0022112094004465>
- Wolff, J.K. and Sharman, R.D. (2008) Climatology of upper-level turbulence over the contiguous United States. *Journal of Applied Meteorology and Climatology*, 47, 2198–2214. <https://doi.org/10.1175/2008jamcl1799.1>

How to cite this article: Wilms H, Bramberger M, Dörnbrack A. Observation and simulation of mountain wave turbulence above Iceland: Turbulence intensification due to wave interference. *Q.J.R. Meteorol. Soc.* 2020;146:3326–3346. <https://doi.org/10.1002/qj.3848>

APPENDIX

A. EULAG equations

The irregularly spaced coordinates (x, y) of the physical domain D_p are mapped onto regularly spaced coordinates (\bar{x}, \bar{y}) of the transformed computational domain D_t using a bijective mapping function

$$(\bar{x}, \bar{y}) \equiv F(x, y) : D_p \rightarrow D_t. \quad (\text{A1})$$

In these generalized coordinates (\bar{x}, \bar{y}) , the anelastic equations read (e.g., Wedi and Smolarkiewicz, 2003; Kühnlein *et al.*, 2012):

$$\frac{dv^j}{dt} = -\tilde{\mathbf{G}}_j^k \frac{\partial \pi'}{\partial \bar{x}^k} + g \frac{\theta'}{\theta} \delta_3^j - \epsilon_{jik} f_i v'^k - \alpha v'^j \equiv \mathcal{R}^j, \quad (\text{A2a})$$

$$\frac{d\theta'}{dt} = -\bar{v}^s \frac{\partial \theta_e}{\partial \bar{x}^k} - \beta \theta' \equiv \mathcal{R}^{\theta'}, \quad (\text{A2b})$$

$$\frac{\partial(\rho^* \bar{v}^s)}{\partial \bar{x}^k} = 0. \quad (\text{A2c})$$

These equations describe the three components of the momentum equation (A2a), the thermodynamic

equation (A2b) and the mass continuity equation (A2c). The indices $j, k = 1, 2, 3$ correspond to the $\bar{x}, \bar{y}, \bar{z}$ components, respectively, and summation over repeated indices is implied (unless stated otherwise). The renormalized elements of the Jacobian matrix are given by $\tilde{\mathbf{G}}_j^k = \sqrt{g^{ij}} \partial \bar{x}^k / \partial x^j$ (g^{ij} are the diagonal elements of the conjugate metric tensor, no summation implied here) and the determinant of the Jacobian matrix is \bar{G} . The generalized density is given by $\rho^* = \bar{\rho} \bar{G}$. The Kronecker delta δ_3^j yields 1 for $j = 3$ (0 otherwise) and ϵ_{jik} is the Levi-Civita symbol. The physical velocities are denoted by v^j , potential temperature by θ , density by ρ and density normalized pressure by π . The symbol \mathbf{g} symbolizes the gravity vector and f_i the components of the Coriolis parameter. The basic state of the anelastic equations (Ogura and Phillips, 1962; Clark and Farley, 1984; Bacmeister and Schoeberl, 1989), denoted by $\bar{\theta}$, $\bar{\rho}$ and $\bar{\pi}$, is prescribed as a horizontally homogeneous and hydrostatically balanced profile with constant stability. A more general environmental state, which reflects the initial and boundary conditions, enter the equations via the variables with subscript e. All primed variables in Equation A2 refer to deviations from the environmental state, i.e. $X' = X - X_e$. The solenoidal velocities \bar{v}^s are obtained through $\bar{v}^s = \tilde{\mathbf{G}}_j^k v^j$. The right-hand side of the equations are abbreviated with \mathcal{R}^Ψ , with Ψ corresponding to v^j and θ' . At the top and lateral boundaries of the modelling domain, damping is achieved by a relaxation towards the environmental state with the damping coefficients α and β . Within the damping layer of thickness δx_{ab} , the damping coefficients increase linearly from 0 to α_0 and β_0 . In the vertical, terrain-following coordinates (Gal-Chen and Somerville, 1975) are used.

The anelastic equations are solved numerically using a non-oscillatory forward-in-time approach of second-order accuracy in space and time, either in Eulerian mode or semi-Lagrangian mode (hence the name EULAG) via

$$\Psi^{n+1} = LE(\Psi^n + 0.5 \Delta t \mathcal{R}^\Psi |^n) + 0.5 \Delta t \mathcal{R}^\Psi |^{n+1}. \quad (\text{A3})$$

LE stands for the Eulerian or semi-Lagrangian transport operator and n for the time step. The simulations presented in this study employ the Eulerian mode by applying the multidimensional positive definite advection transport algorithm (MPDATA; Smolarkiewicz and Margolin, 1998; Smolarkiewicz, 2006). The elliptic pressure equation is solved via a preconditioned non-symmetric Krylov subspace solver (Smolarkiewicz and Margolin, 1994; 1997, Skamarock *et al.*, 1997). A comparison between different well-established numerical models (including EULAG),

and their capability to model flow over steep terrain, appears in Doyle *et al.* (2011).

EULAG has several options for subgrid-scale models, including a Smagorinsky closure model and a prognostic equation of the turbulent kinetic energy (Sorbjan, 1996). Additionally, EULAG can be run as implicit large-eddy simulation (ILES; Grinstein *et al.*, 2007), where the truncation error of the discretization is exploited to model the effects of subgridscale motions. This ILES setting is employed in this study.

B. Grid stretching

The stretched grid (x,y) in the physical domain \mathcal{D}_p is obtained through a mapping function from the regularly spaced generalized coordinates (\bar{x},\bar{y}) in the computational

domain \mathcal{D}_t . The mapping function is based on a fifth-order polynomial function

$$x(\bar{x}) = c_x[a_1(\bar{x} - \Delta_x) + a_2(\bar{x} - \Delta_x)^5] + b_x, \quad (\text{B1})$$

which takes the analogous form for $y(\bar{y})$. The polynomial terms are weighted equally ($a_1 = a_2 = 0.5$), and the further parameters ($c_x = 0.997$, $\Delta_x = 0.026$, $b_x = 0.078$, and likewise $c_y = 0.999$, $\Delta_y = -0.015$ and $b_y = -0.045$ for $y(\bar{y})$) shift the region of highest resolution towards the position of the turbulence encounter. The generalized coordinates (\bar{x},\bar{y}) must be normalized to the interval $[-1,1]$ before applying the grid stretching function (Equation B1). The returned grid (x,y) is likewise normalized to $[-1,1]$, so that it is then rescaled to the original size.